JOURNAL OF GEOPHYSICAL RESEARCH, VOL. 92, NO. C7, PAGES 6754–6772, JUNE 30, 1987

Mesoscale Eddies in the Fram Strait Marginal Ice Zone During the 1983 and 1984 Marginal Ice Zone Experiments

J. A. JOHANNESSEN,[1] O. M. JOHANNESSEN,[1,2] E. SVENDSEN,[1] R. SHUCHMAN,[3] T. MANLEY,[4] W. J. CAMPBELL,[5] E. G. JOSBERGER,[5] S. SANDVEN,[1] J. C GASCARD,[6] T. OLAUSSEN,[1] K. DAVIDSON,[7] AND J. VAN LEER[8]

During the summer Marginal Ice Zone Experiment in Fram Strait in 1983 and 1984, fourteen mesoscale eddies, in both deep and shallow water, were studied between 78° and 81°N. Sampling combined satellite and aircraft remote sensing observations, conductivity-temperature-depth observations, drift of surface and subsurface floats and current meter measurements. Typical scales of these eddies were 20–40 km. Rotation was mainly cyclonic with a maximum speed, in several cases subsurface of up to 40 cm s^{-1}. Observations further suggest that the eddy lifetime was at least 20 to 30 days. Five generation sources are suggested for these eddies. Several of the eddies were topographically trapped, while others, primarily formed by combined baroclinic and barotropic instability, moved as much as 10–15 km d^{-1} with the mean current. The vorticity balance in the nontrapped eddies is dominated by the stretching of isopycnals accompanied by a change in the radial shear. In the most completely observed eddy south of 79°N the available potential energy exceeded the kinetic energy by a factor of 2. Quantitative estimates suggest that the abundance of these eddies enhances the ice edge melt up to 1–2 km d^{-1}.

1. INTRODUCTION

The marginal ice zone (MIZ) is the transition region from open ocean to pack ice. Here strong mesoscale air-ice-ocean interactive processes occur which control the advance and retreat of the ice margin. To gain better understanding of these processes, the 1984 Marginal Ice Zone Experiment (MIZEX '84) was carried out in Fram Strait between Greenland and Svalbard from May 18 to July 30, 1984, following a preliminary summer experiment in 1983 [*MIZEX Group*, 1986]. One of the central objectives of MIZEX is to understand the physics of mesoscale eddies and their importance in the various exchange processes of mass, heat, and momentum which affect the position of the ice edge.

Major investigations of mid-ocean eddies started in 1973 with the Mid-Ocean Dynamics Experiment (MODE) 1 program [*Robinson*, 1983]. Although it is now well established that eddies are present in all the world oceans with important implications for physical, biological, chemical, and geological oceanography and acoustics [*Robinson*, 1983; *Magaard et al.*, 1983], eddy features have not been extensively investigated in the MIZ. To qualitatively demonstrate the effect of eddies in the MIZ, a unique aerial photograph obtained on June 30, 1984 is shown in Plate 1, where the ice traces the cyclonic orbital motion of an eddy at the ice edge. (Plate 1 is shown here in black and white. The color version can be found in the separate color section in this issue.) Such motion advects large amounts of ice, Polar Water (PW), and Atlantic Water (AW) into closer contact, causing enhanced floe breakup and ice melting. While Plate 1 shows one ice edge eddy in detail, the National Oceanic and Atmospheric Administration (NOAA) satellite image from July 1, 1984 (Plate 2) establishes that eddies and meanders are the dominant features along the ice edge under moderate wind conditions. (Plate 2 is shown here in black and white. The color version can be found in the separate color section in this issue.) Note also the large number of eddies in the ocean off the ice edge.

Fram Strait is the region where almost all heat and water exchange between the Arctic Ocean and the Atlantic Ocean takes place [*Aagaard and Greissman*, 1975]. The general large-scale ocean circulation in this region is dominated by the southward flowing cold and low-salinity East Greenland Current (EGC) which exports ice and PW out of the Arctic Ocean, and the northward flowing warm and saline AW in the West Spitzbergen Current (WSC) [*Perkin and Lewis*, 1984]. The West Spitzbergen Current separates into filaments that either recirculate in Fram Strait or advect AW into the Arctic (Figure 1). The large-scale ocean circulation studied during MIZEX '84 is reported by *Quadfasel et al.* [this issue]. Three distinct water masses characterize the upper 1000 m in Fram Strait. *Swift and Aagaard* [1981] and *Swift* [1986] defined these water types as follows: Polar Water (salinity $S < 34.4$‰, temperature $T >$ freezing), Atlantic Water ($A > 34.9$‰, $T > 3°$C), and Arctic Intermediate Water (AIW) ($34.4 < S < 34.9$‰, $0 < T < 3°$C). Thermal and saline ocean fronts and eddies form where these water masses interact.

Fram Strait has a complicated bathymetry, as is shown in Figure 1. The continental shelves of Svalbard and Greenland border each side of the strait. The Yermak Plateau with a mean depth of 800 m extends northwestward from Svalbard. The most dramatic variations are found in the central part of Fram Strait where there are several deep depressions, such as Molloy Deep, which extends to 5500 m, while seamounts and ridges rise steeply to about 1500 m below the surface.

Previous investigation in Fram Strait have revealed that mesoscale eddies are present along the ice edge [*Johannessen et al.*, 1983; *Wadhams and Squire*, 1983, *Vinje*, 1977]. The

[1] Nansen Remote Sensing Center, Bergen, Norway.
[2] Geophysical Institute, University of Bergen, Bergen, Norway.
[3] Environmental Research Institute of Michigan, Ann Arbor.
[4] Lamont-Doherty Geological Observatory, Columbia University, Palisades, New York.
[5] U.S. Geological Survey, University of Puget Sound, Tacoma, Washington.
[6] Laboratoire d'Océanographie Physique, Muséum d'Histoire Naturelle, Paris.
[7] Naval Postgraduate School, Monterey, California.
[8] Department of Oceanography, University of Miami, Florida.

Paper number 7C0113.
0148-0227/87/007C-0113$05.00

Plate 1. Aerial photograph of the 20- to 40-km ice edge eddy E1 centered at 79°N, 2°30'W taken from the CV 580 on June 30, 1984. (The color version of this figure can be found in the separate color section in this issue.)

scales of these eddies ranged from 5–15 km north of Svalbard to 50–60 km for the Molloy Deep eddy in the central part of Fram Strait. The generation mechanisms which have been suggested for these eddies are summarized in Table 1, together with horizontal and vertical eddy scales, estimated or measured orbital speed, and eddy propagation speed. The mechanisms include barotropic and baroclinic instability, topographic trapping, differential Ekman pumping along the ice edge, and ice edge instability driven by internal ice dynamics. The topographyically controlled eddy over Molloy Deep has also been simulated in a numerical model [*Smith et al.*, 1984], while upper ocean eddies along the ice edge with scales of 20–40 km are generated by differential Ekman pumping in a numerical model by *Häkkinen* [1986]. Moreover, the internal ice stress can also generate instability of an infinite sea ice front overlying a passive ocean as modeled by *Killworth and Paldor* [1985].

MIZEX '83 and MIZEX '84 used a variety of observational techniques to study open ocean eddies, eddies at the ice edge, and eddies beneath the ice. These techniques include satellite and aircraft remote sensing, standard conductivity-temperature-depth (CTD) sections from ships and helicopters, the drift of surface and subsurface floats, current meter measurements, and Cyclesonde measurements [*MIZEX Group*, 1986]. The combination of all of these data sources provides a detailed picture of eddies in the MIZ. This study describes first the eddies south of 79°N, then the eddies in the central part of Fram Strait between 79° and 80°N, followed by the eddies north of 80°N, and concludes with a discussion of eddy sources, vorticity, energy, and eddy-induced ablation and ice edge retreat in the MIZ. In all, 14 eddies, E1 to E14, are discussed in the following.

2. Description of the Eddy Data

The ice-ocean eddy program was carried out along the ice edge from 81°N, north of Svalbard, to 78°N. We will describe the eddy observations in three sequences; south of 79°N, between 79° and 80°N, and north of 80°N.

2.1. *South of 79°N*

This program lasted from July 4 to 15, 1984, with the research vessel *Håkon Mosby* covering the open water part of the eddy region and the research vessel *Kvitbjørn* covering the ice part, in conjunction with repeated remote sensing aircraft overflights. Figure 2*a* shows the passage of three low-pressure systems through Fram Strait with maximum winds up to 20 m s^{-1}, and Figure 2*b* shows the associated ship-measured wind conditions from June 15 to July 15. The mean ice edge is also superimposed on the weather maps and indicates that along

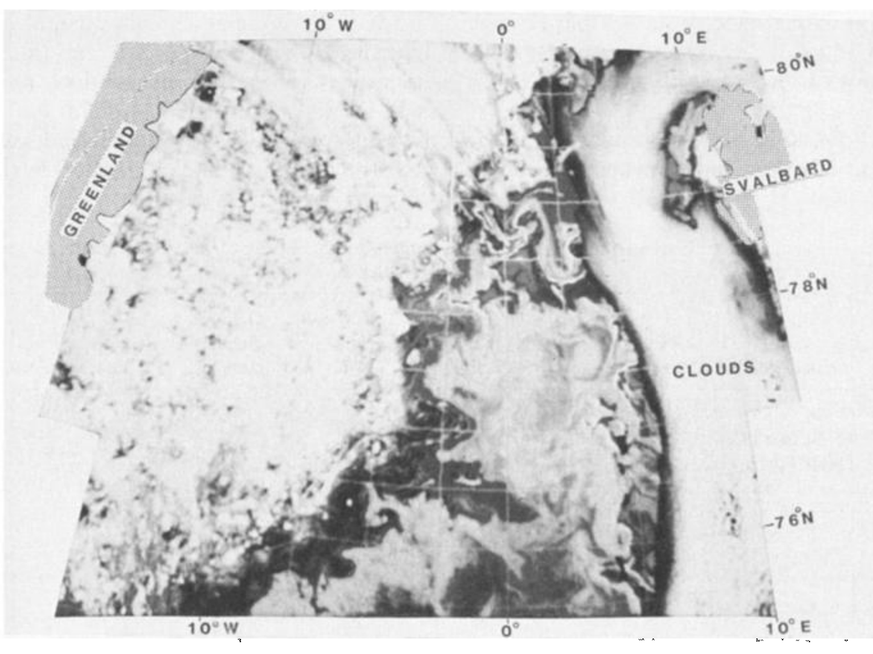

Plate 2. NOAA satellite AVHRR image (combined IR and visual) from July 1, 1984. (The color version and a complete description of this figure can be found in the separate color section in this issue.)

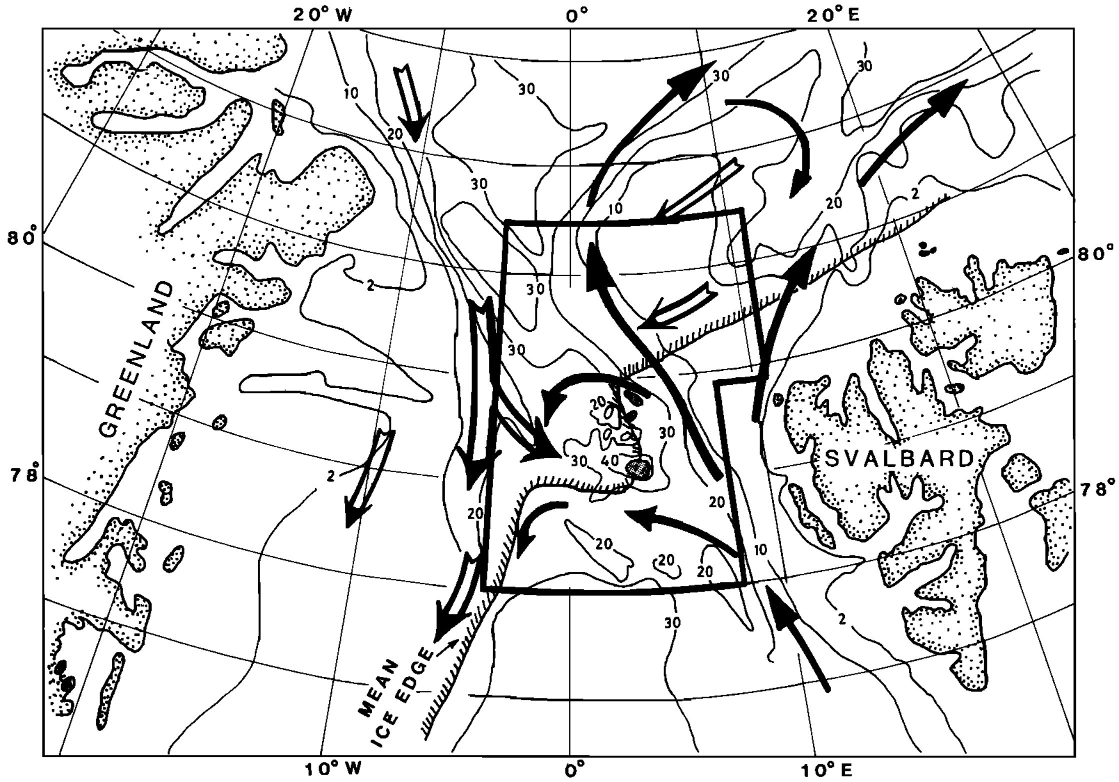

Fig. 1. Fram Strait bathymetry (depth in hundreds of meters), mean summer ice edge (hatched) and general upper ocean circulation (solid arrows indicate flow of Atlantic Water, open arrows indicate ice drift and flow of Polar Water). The main experimental site is located within the marked box.

ice edge winds with the ice to the right (looking downwind) often occur during the passage of low-pressure systems.

A total of 250 conductivity-temperature-depth (CTD) stations were obtained from the two ships, with typical station spacing of 4 km and a sampling depth of 500 m (Figure 3). Furthermore, the research vessel *Polarstern* carried out a west-east section and a north-south section to the bottom through the region on July 7–8 and July 16, 1984, respectively, while R/V *Kvitbjørn* later repeated the two sections on July 21–22, (Figure 3).

The eddy features, E1–E4, to be discussed are shown in the sequence of satellite and aircraft remote sensing images obtained between June 26 and July 14, 1984 (Plates 3*a* and 3*b*). (Plate 3*a* is shown here in black and white. The color version can be found in the separate color section in this issue.) On June 26 the ice edge eddy E1 started to form at approximately 79°15′N and 1°30′W (Plate 3*a*) and was fully developed on June 29 with a scale of 20–40 km centered at about 79°N and 2°15′W. This suggests a spinup time of about 3 days for the upper layer which contains PW and ice. During these 3 days the mean southward propagation of the eddy deduced from these images was 10 km d^{-1} (1 km $d^{-1} \approx 1$ cm s^{-1}). When this eddy was first observed, the wind was along the ice edge from the northeast 20 m s^{-1}, later decreasing in speed and

TABLE 1. Generation Mechanisms for Mesoscale Eddies in the Fram Strait, in Addition to Some Eddy Characteristics

Generation Mechanism	Horizontal Scale, km	Vertical Scale, m	Orbital Speed, cm s^{-1}	Propagation
Barotropic instability, Norsex '79 [*Johannessen et al.*, 1983]	5–15	<200	5–20	10 cm s^{-1}
Molloy Deep Eddy				
Baroclinic instability, Ymer 80 [*Wadhams and Squire*, 1983]	60	>600	7–16	negligible
Topographic controlled, MIZEX '83 [*Johannessen et al.*, 1984]	50–60	>2000	15–25	stationary
Topographic controlled, Numerical model [*Smith et al.*, 1984]	60–80	3500	50	stationary
Häkkinen [1986]	10–40	<100		nonlinear advection
Killworth and Paldor [1985]	20–50	no ocean		

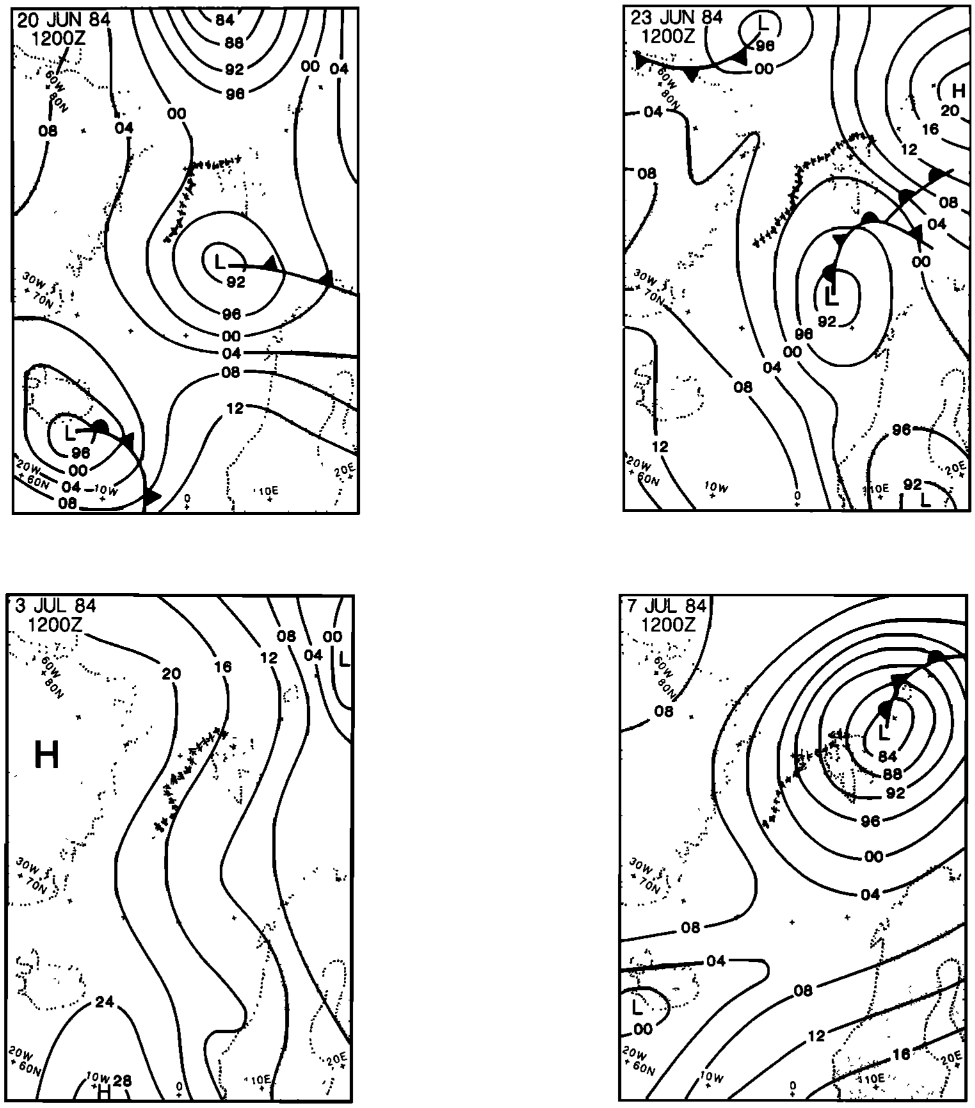

Fig. 2a. Pressure maps on June 20 and 23 and July 3 and 7, 1984 (values in millibars, two last digits). The hatched line indicates mean ice edge.

backing to the north. From June 29, to July 1, E1 moved slowly southwards towards 78°50′N and 2°W, while the apparent motion between July 1 and 4 was slowly eastward. In all, the propagation of E1 is controlled mainly by the background motion, since the self-propagation of eddies at high latitudes is negligible [*Johannessen et al.*, 1983]. In contrast, two large ice floes were recognized about 15 km to the west of this eddy with a mean southward drift of 30 cm s^{-1} between June 26 and July 4.

The spinup of a second eddy, E2, 50 km southwest of E1 occurred between July 1 and 4. In this period, intensification of the high pressure Figures 2*a* and 2*b* led to north to northeast winds reaching 12 m s^{-1}. The July 4 IR image also shows the presence of the eddy features E3 and E4 in the AW just off the ice edge.

The synthetic aperture radar (SAR) mosaic obtained on July 5 (Plate 3*b*) as well as the aircraft photo obtained on June 30 (Plate 1) clearly revealed the detailed surface stucture of the elliptically shaped eddy E1 with dimensions of 20–40 km. Since the wind conditions during these 2 days were relatively calm, and the ice concentration in the eddy was low (less than 50%), implying negligible internal ice stress [*Røed and O'Brien*, 1983], the ice mirrors the upper ocean circulation. The orbital motion, at least in the surface layer, is cyclonic, while the pattern of spiraling lines of ice toward the center implies that ageostrophic effects are important. The primary effect is assumed to be associated with frictionally driven inward radial motion and convergence in the surface layer. However, the effect of surface tilt may also lead to inward radial motion.

In contrast to the SAR mosaic on July 5, the July 7 mosaic reflects the ice configuration influenced by 2 days of strong northerly winds of up to 15 m s^{-1}. This wind event erased the clear ice convergence signature within the eddy but did not completely erase the ice boundary signature, demonstrating that imaging radars can observe ice-ocean eddies even under high wind conditions. Prevailing northerly winds of 5 m s^{-1} on July 8 and 9 again allowed the ice to reflect the upper ocean current, as can be seen in the SAR mosaic obtained on July 9. The center position of this eddy is almost the same as that observed on July 5. There also appears to be another eddy present in the northeast corner of this mosaic, which is

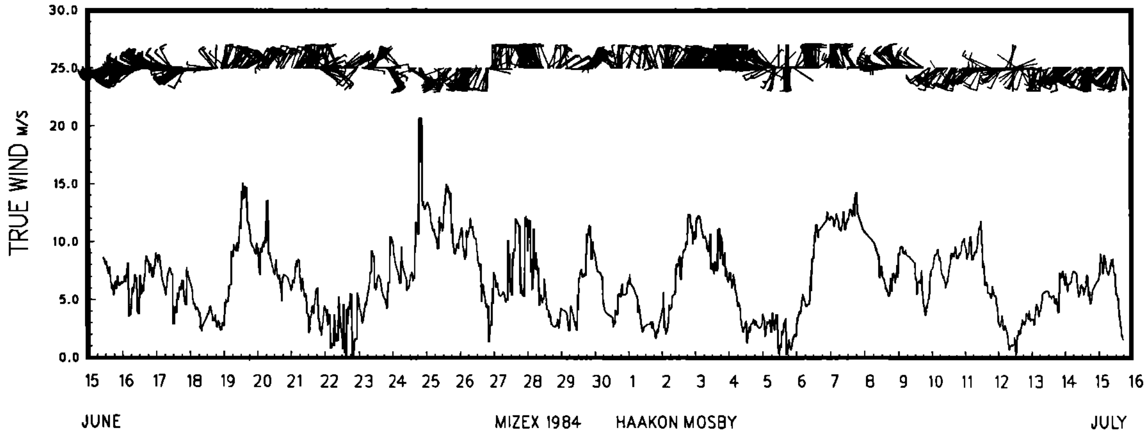

Fig. 2*b*. Wind observations (30-min averages) obtained from R/V *Håkon Mosby* between June 15 and July 15 1984.

the eddy E4 in Plate 3*a*. The winds of less than 8 m s^{-1} from July 12–14 again allowed E1 to be seen in the July 14 side-looking airborne radar (SLAR) mosaic (Plate 3*b*).

The three-dimensional temperature composite (Plate 4) derived from the star pattern CTD sections (Figure 3) obtained during the period July 10–14, 1984, shows the complex subsurface structure of eddies E1 and E3. (Plate 4 is shown here in black and white. The color version can be found in the

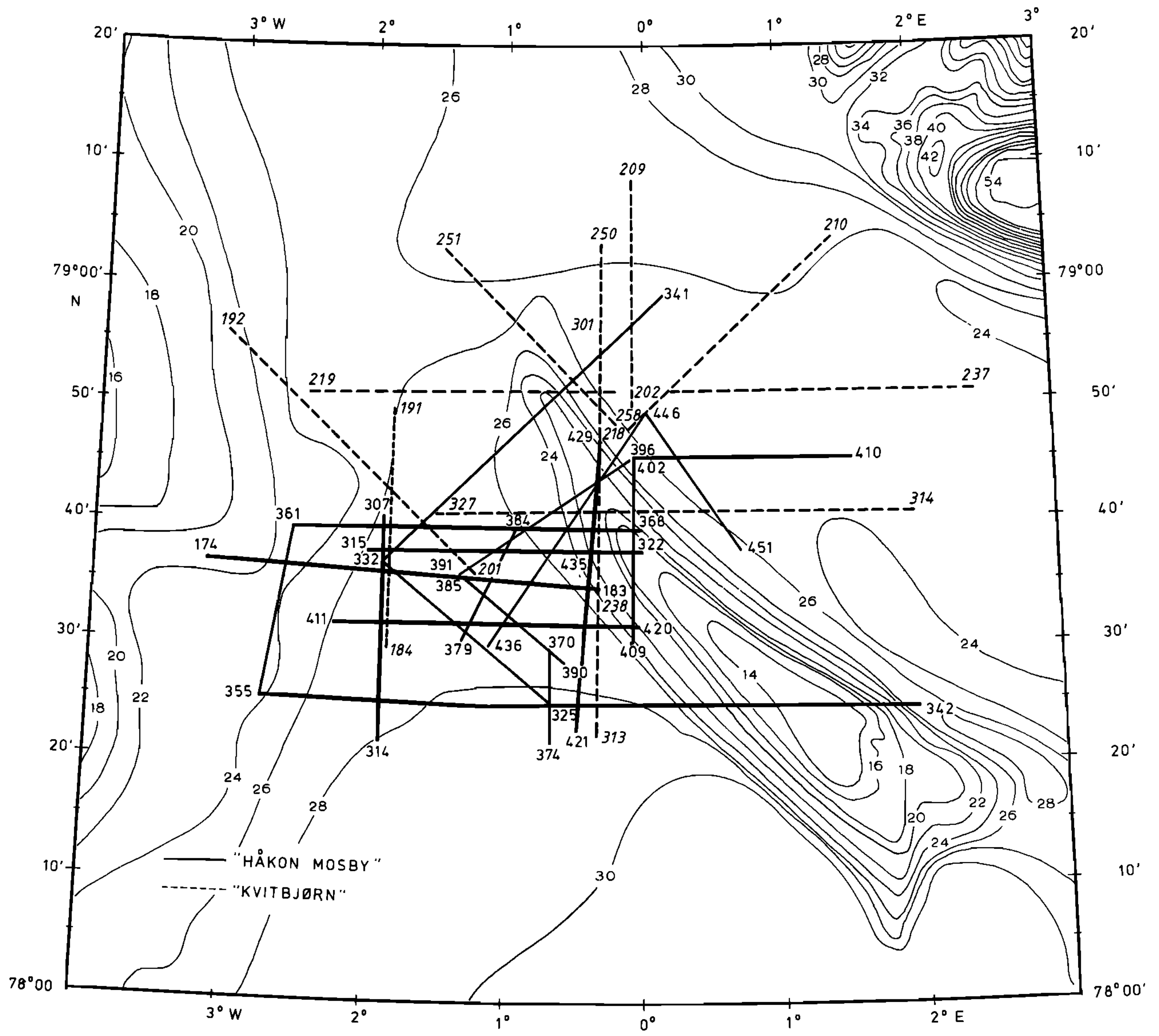

Fig. 3. CTD station map from July 4 to 14, 1984, giving start and end station numbers for each CTD section together with bathymetry (contour interval of 200 m).

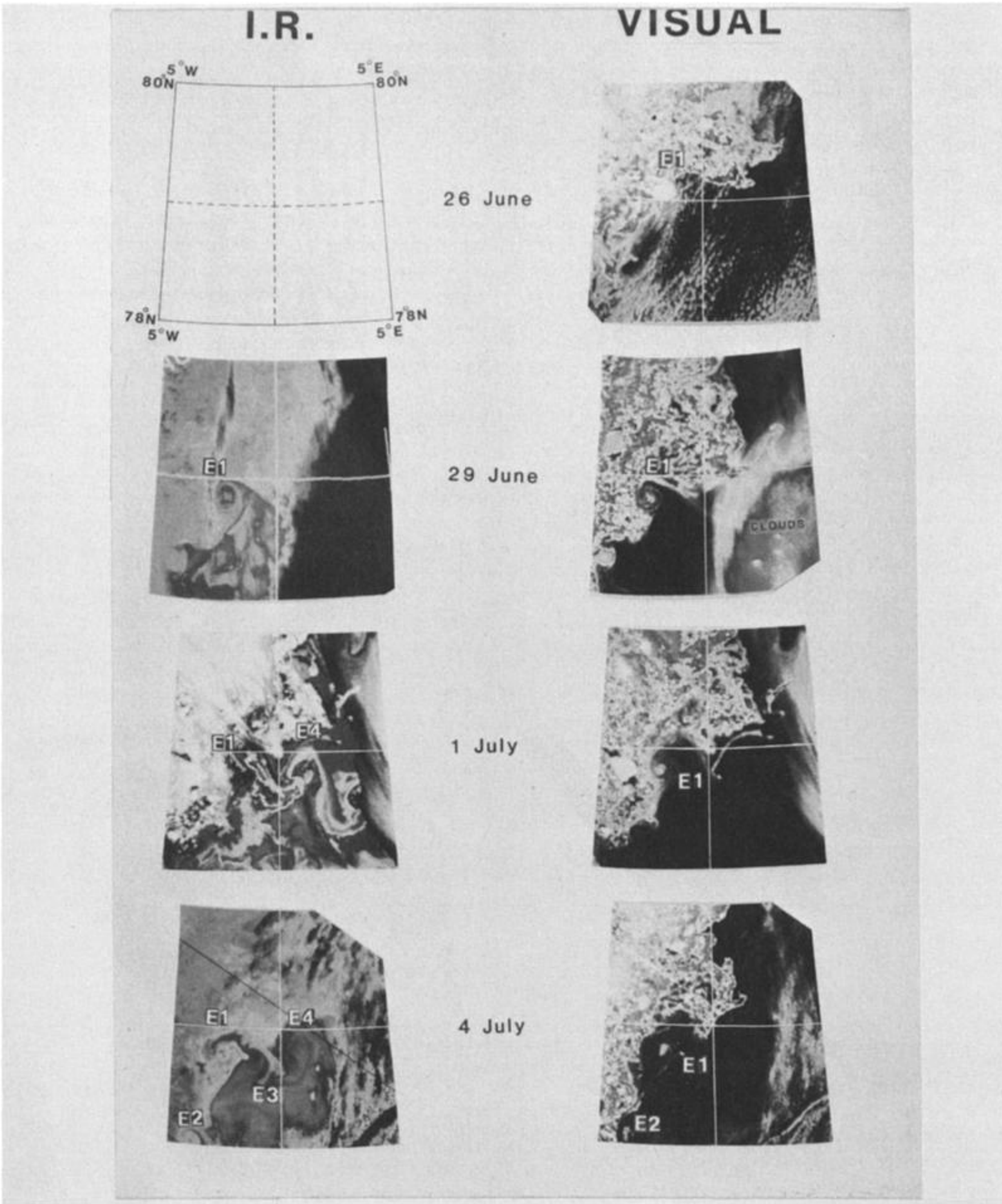

Plate 3a

Plate 3. Sequence of NOAA satellite visual and IR images on June 26, June 29, July 1, and July 4; aircraft SAR mosaics on July 5, 7, and 9; and SLAR mosaic on July 14. Eddy features labeled E1–E4 are discussed in the text. (The color version of this figure can be found in the separate color section in this issue.)

separate color section in this issue.) The structure of E3, documented by CTD stations, included in the three-dimensional composite in Plate 4, shows a vertical doming of about 300 m with cyclonic rotation. Repetitive CTDs through the eddy center of E1 over this 5-day period, showed that the eddy remained stationary, verifying the synoptic representation of Plate 4. The blue color in the upper layer represents the PW with temperature less than 2°C, while the red color is AW with temperature above 4°C. Ice is shown by the white spots, while the blue color in the interior represents water temperature below 2°C. The mean movement of the ice and PW is indicated by arrows which show the westward drift in the northern domain and the sudden cyclonic turn southward at the edge of the EGC. Similarly, the mean drift of the AW is shown by arrows. Significant dome structure appeared beneath the surface layer of the eddies. This indicates that the vertical depth of the eddies exceeds 500 m. The winds during this period were consistently southwest at 5–10 m s^{-1}, with no major influence on the structure of the eddies. A section obtained on July 16, 1984 by R/V *Polarstern* showed that the eddy density anomaly disappeared below 1000 m.

A more detailed view of the structures of E1 and E3 can be seen in the east-west and north-south CTD sections shown in Figures 4*a*–4*d*. The east-west section (Figure 4*a*) shows warm AW (>4.5°C) extending from a core depth of 50 m to the surface centered above the interior dome structure. The north-south section (Figures 4*b* and 4*d*) shows similar interior dome structure in the vicinity of the eddy center with the main core of AW located above. However, the surface manifestation is weaker, with temperature below 3.5°C.

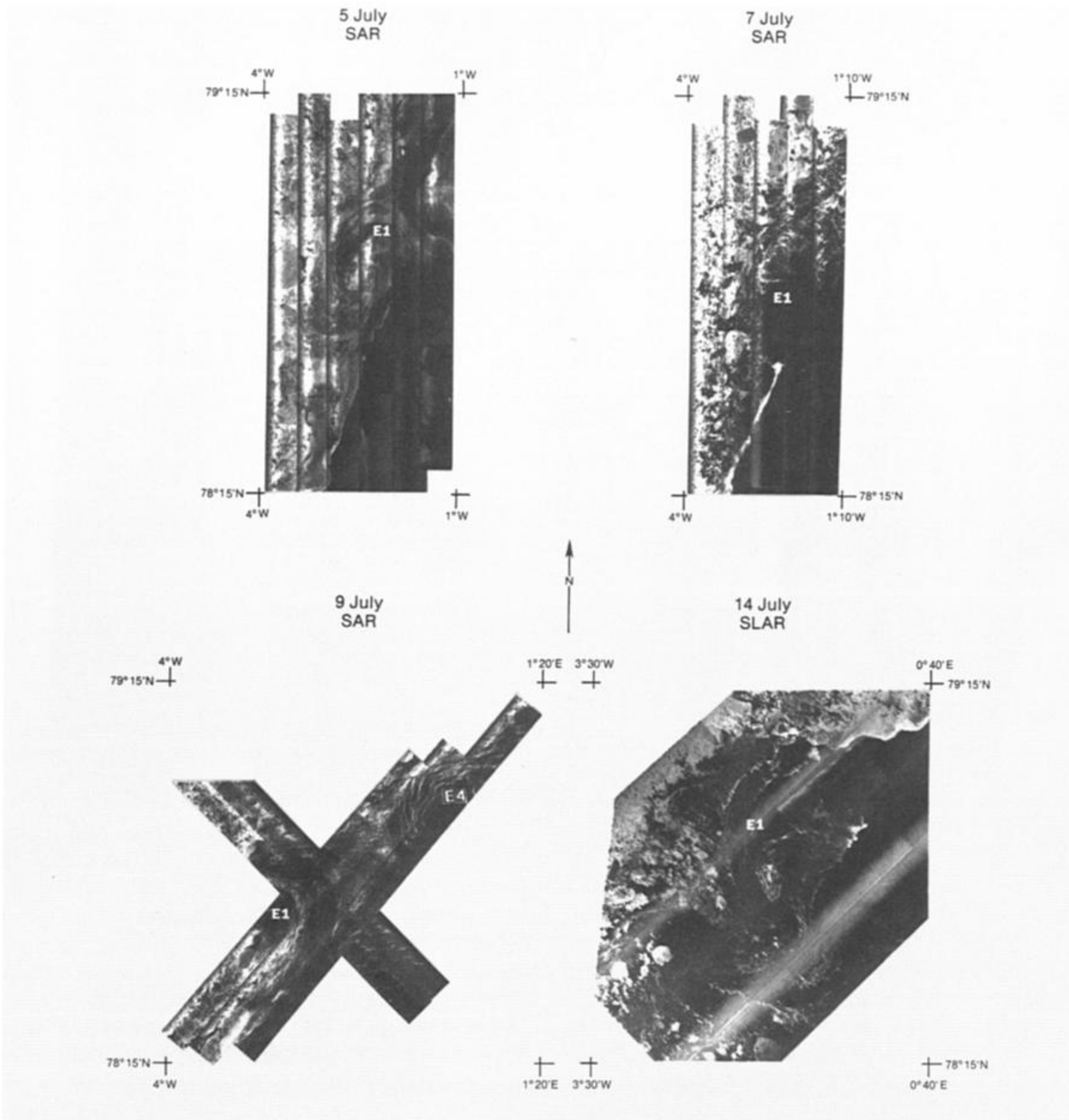

Plate 3b

In addition to the central core of AW located near the eddy center, a filament of AW is located to the west of the eddy center at a depth of 50 m (Figure 4*a*, at station 224), and to the north of the eddy center at a depth of 60 m (Figure 4*b*, at station 249) on July 13. This filament acts as a tracer. It was first observed 30 km northeast of the eddy center on July 11, with a width of about 10 km at a mean depth of 50 m. It was also found in the section obtained on July 14, at a mean depth of 30 m, about 20 km northwest of the eddy center. This filament displayed a cyclonic motion around the eddy center, and if it is continuous, the calculated orbital speed is about 50–70 cm s^{-1}, which is higher than the direct current measurements reported below.

The velocity field was derived by drifting Argos buoys, one of which had current meters suspended below it. The drift pattern of Argos buoy 5062 deployed on an ice floe in the eddy E1 on July 9 is shown in Figure 5 together with absolute current vectors at 5, 10, and 50 m. During July 10 the ice floe and the buoy were forced by the wind from southwest across the warm core of the cyclonically turning AW which had maximum velocities at 50 m of more than 40 cm s^{-1}. After going through some small-scale anticyclonic rotation, perhaps associated with eddy-eddy interaction, the buoy enters the strong southward current associated with the eddy E4 on July 11. Early on July 12 the northern current weakens and turns cyclonically to flow east-northeast in agreement with the surface structure of E4 seen in the remote sensing images (Plates 3*a* and 3*b*). There was no dramatic change in the magnitude of the current vectors during the 4-day period, which suggests that the eddy orbital speed in E1 and E4 is similar for the upper 50 m, of the order of 30–40 cm s^{-1}.

The observed vertical shear exhibits a weak increase of 10^{-3} s^{-1} in the upper 50 m (Figure 5) in agreement with subsurface maximum seen in the geostrophic flow calculations with level of no motion at 500 m (Figure 6). The subsurface maxima of 20 cm s^{-1} present in E1, result from the reversal of the slope

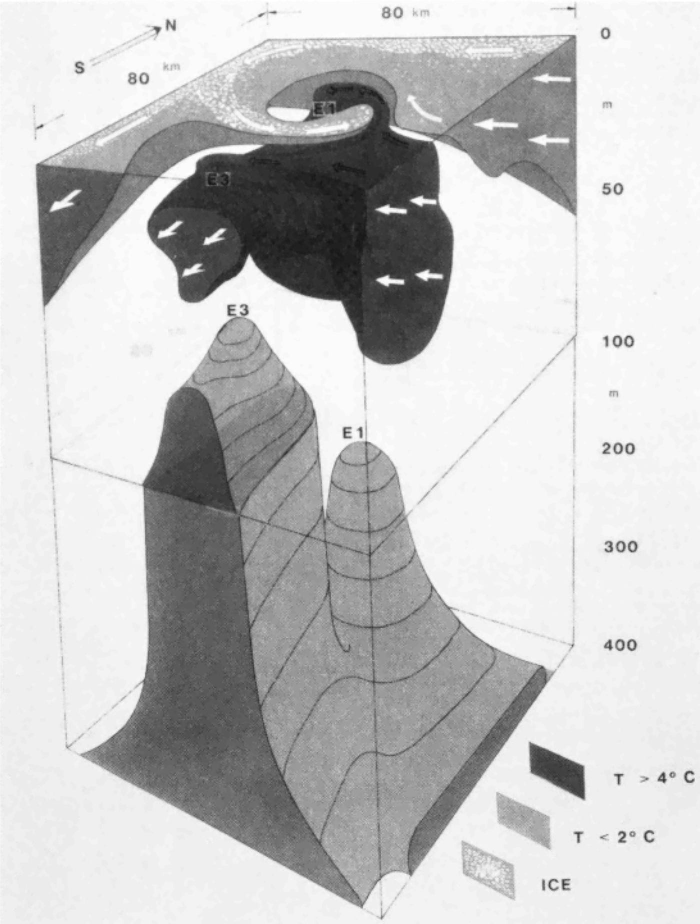

Plate 4. Three-dimensional temperature composite of E1 and E3. Arrows indicate the motions of the ice, Polar Water, and Atlantic Water. (The color version of this figure can be found in the separate color section in this issue.)

of the isopycnals in the upper layer (Figures 4*c* and 4*d*). This maximum suggests that the barotropic speed in E1 (and E4) is 10–20 cm s^{-1}. On the other hand, the vertical shear was of the order of 10^{-3} s^{-1}, in agreement with that obtained from the current meters. Furthermore, the northern part of the open ocean eddy E3 has a surface maximum speed of about 25 cm s^{-1} at station 424 (Figure 6), while the horizontal and vertical shear are of the same magnitudes as for E1.

The trajectory of buoy 5071 from July 9–11 (Figure 5), deployed in open water in the vicinity of the eddy E4 with a 3 m by 3 m sail centered at 10 m, similarly displays the orbital motion associated with the cyclonic eddy E4. The estimated speed of this buoy was 30 cm s^{-1}, in agreement with the later observation on July 12 by the current meter suspended from buoy 5062. The geostrophic calculations with level of no motion near the bottom at 2500 m using the July 16 north-south R/V *Polarstern* CTD section gave maximum cyclonic orbital speed at the surface of 35 cm s^{-1} in E4 in good agreement with the buoy drift speed. Moreover, the vertical shear was mainly confined to the upper 500 m.

The drift of buoy 5090 located in open water without sail is shown in Figure 5 together with the SLAR mosaic obtained on July 16. From July 10 to 15 the buoy drifted around the periphery of E1 and E4; subsequently, it was caught in the cyclonic rotation of E1, with a radius of about 20 km and an orbital speed of 30 cm s^{-1}. After July 18 the buoy continued its orbital motion with a period of 2.5 to 3.5 days, while being advected in the mean southward flow of the same magnitude as the eddy orbital speed, implying that the eddy E1 started to propagate after July 15. After July 29, south of 78°N the buoy accelerated and made two open loops before the eddy signal in the drift path disappeared. This indicates an eddy lifetime in the surface layer of at least 20–30 days (the subsurface eddy signature may persist longer) with a mean motion of 15 km/d^{-1}.

2.2. *Between 79° and 80°N*

In the central part of Fram Strait the complex bathymetry, including Molloy Deep, affects the barotropic component of the ocean circulation. The cyclonic recirculation of the AW (E5) is coupled to this complex bathymetry. The idea that the positive relative vorticity is further enhanced by the deepening of the AW core as if flows underneath the PW addes new insight into the recirculation of AW. A schematic of this AW recirculation is shown in Figure 7, together with the bathymetry, location of a north-south CTD section, and trajectories of drifting buoys. The AW deepens and turns westward near 80°N following the isobaths and continues southward where a branch separates eastwards, thus completing a large cyclonic turn in the southern part of Molloy Deep. This is the area where a major ice tongue is often observed in advanced very high resolution radiometer (AVHRR) and passive microwave images (Plate 2) indicating that the recirculated AW drags on the PW and ice to the east. The mesoscale eddies in this area are influenced not only by the regional circulation but also by the complex mesoscale bathymetry.

The north-south CTD section (Figure 8) from July 1–2, 1984, shows the temperature (left) and density (right) structure to the bottom across the central Fram Strait. The regional recirculation as schematically shown in Figure 7 is clearly documented by the core of warm AW at both ends of the section. Also seen is the thin lens (25 m deep) of light trapped PW at the surface (Figure 8, top right). In the interior the deepening of the isopycnals centered at stations 262, 268, and 273 is associated with the topographic depressions, while the doming of the isopycnals centered at station 267 and 271 is associated with the topographic highs. Assuming weak increasing velocity with depth, this may indicate that there are three cyclonic eddies (E6, E8, and E10) and two anticyclonic eddies (E7 and E9) which are topographically controlled in agreement with conservation of potential vorticity on an f plane (Figure 8, bottom right). E6 is the Molloy Deep eddy observed by *Johannessen et al.* [1984] and modeled by *Smith et al.* [1984]. The lack of coupling in the upper 25 m (Figure 8) probably results from wind forcing and stratification.

The cold subsurface core at station 264 of PW possibly results from the anticyclonic circulation indicated by the splitting of the ice tongue, seen in aircraft microwave observations made in 1983–1984. This anticyclonic turn was also recognized in the Argos buoy trajectories. It may result from the sharp curvature of the isobaths which the east-southeastward flow cannot follow. Instead, it is forced upward by the trough, creating negative vorticity resulting in anticyclonic motion. The westward flow of recirculated AW directly to the south of this ice tongue is another source for this negative vorticity.

In 1983, two buoys (T7 and T8) suspended with current

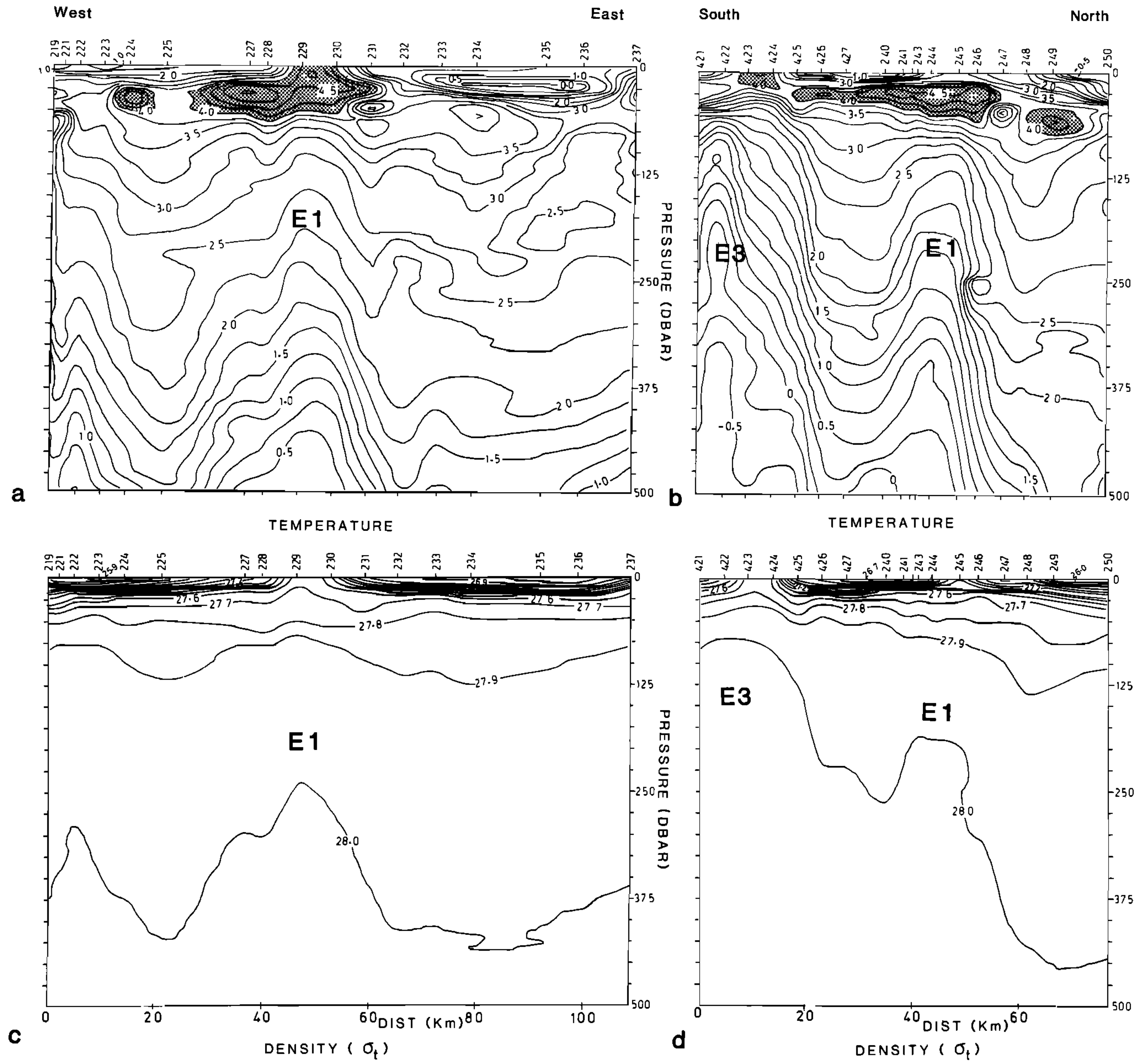

Fig. 4. (*a*, *b*) Temperature and (*c*, *d*) density structure from CTD stations 219–237 and from stations 421–427 and 240–250 indicated at the top of the sections. Water temperature of 4°C or more is shaded.

meters at 2, 10, 20, 40, and 200 m were deployed on ice floes west of Molloy Deep (Figure 7). Direct current measurements from the eastern buoy T7 gave a speed of 20 cm s^{-1} with negligible vertical shear. In comparison, the calculated geostrophic speed in the region with level of no motion at the surface increased to 15 cm s^{-1} at 500 m with weak shear in the first 200 m. This may indicate that the orbital speed in the eddy E6 was about 35 cm s^{-1} at 500 m, with near-equal magnitude of the baroclinic and barotropic flow components.

In 1984, two SOFAR floats (S2 and S7), at 250 m and 725 m showed the combined effects of mesoscale and regional flow (Figure 7). The float at 725 m followed the isobath in the southern part of Molloy Deep with a mean speed of 10 cm s^{-1}. On the eastward side, the float drifted northward out of the deep, probably caught in the regional AW circulation associated with E5. The float at 250 m located in the vicinity of the large seamount north of Molloy Deep made, as was expected, an anticyclonic turn with an average speed of 5 cm s^{-1}. However, the turn gradualy weakens and shifts toward a cyclonic turn as the float is advected across deepening isobaths. The increasing speed with depth as well as the drift trajectories relative to the bathymetry support the above thesis of bathymetric steering. In comparison, the geostrophic speed above 750 m (level of no motion at the surface) were below 5 cm s^{-1} at the crossover points (Figures 7 and 8). Assuming minor time variations in the eddy orbital speed from the SOFAR float measurements to the CTD-inferred geostrophic speed estimates, the results again suggest near-equal magnitude of the baroclinic and barotropic flow components at 750 m.

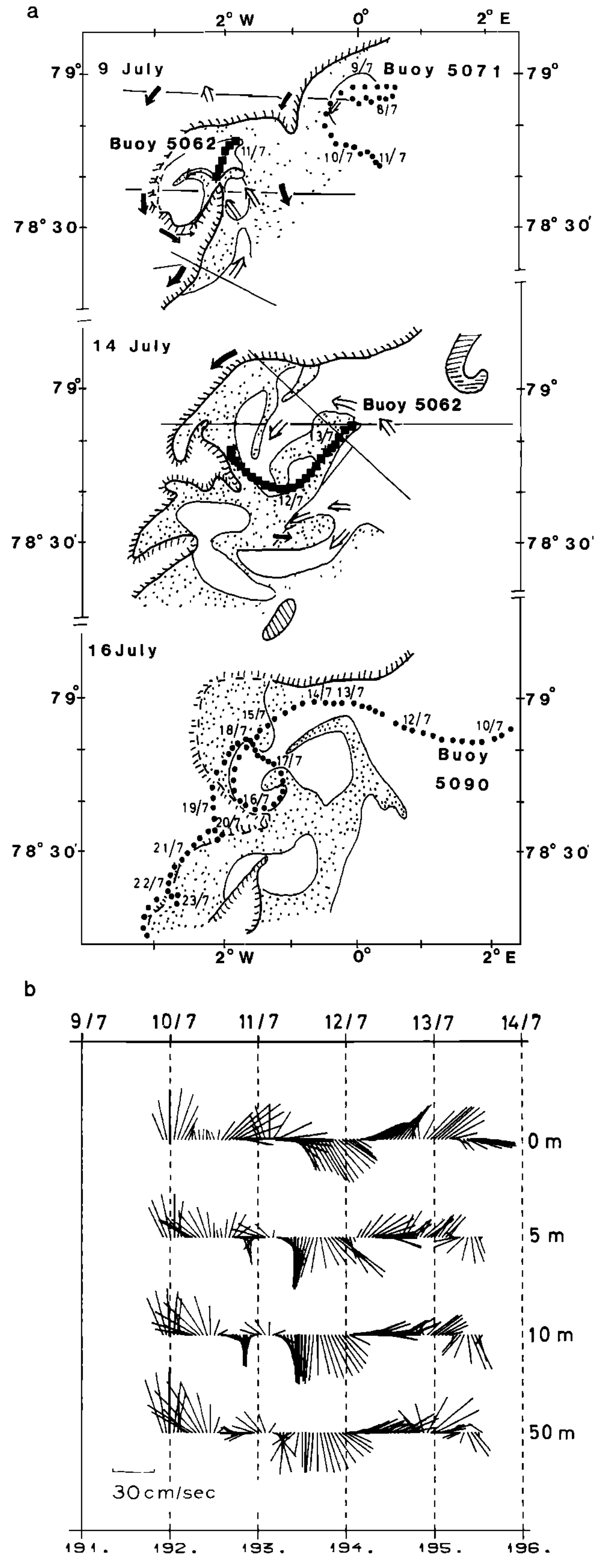

Fig. 5. (*a*) Schematic interpretations of the July 9 SAR and the July 14 and 16 SLAR mosaics. The main ice edge is hatched, and the dotted regions indicate areas with small floes. The trajectories of Argos buoy 5071 (solid dots), buoy 5062 (solid squares), and buoy 5090 (solid dots) are shown. Arrows indicate geostrophic flow of AW (open) and ice and PW (solid). (*b*) Absolute current measurements.

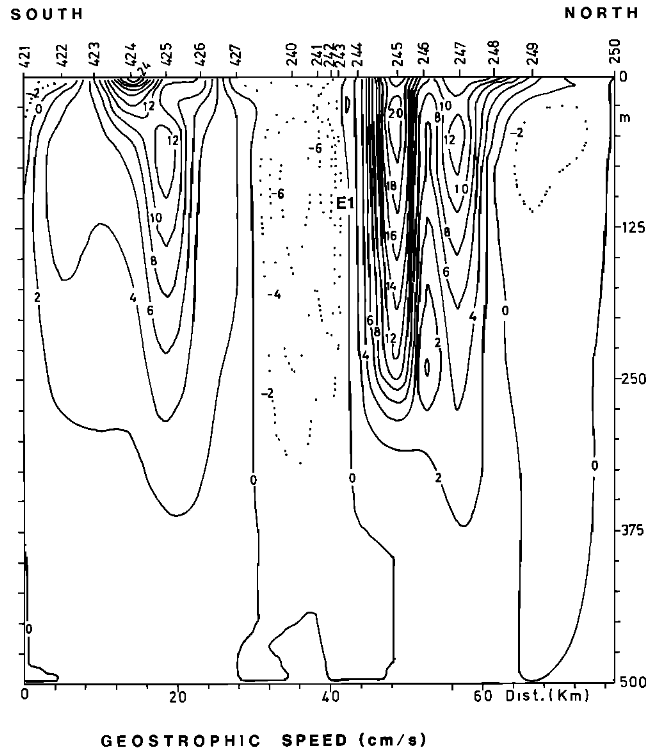

Fig. 6. Geostrophic speed (centimeters per second) from CTD stations 421–427 and 240–250 indicated at the top of the section. Westward speed is shown by solid lines.

2.3. *North of 80°N*

In addition to the influence of the complex bathymetry on the deep water circulation between 79°N and 80°N, evidence of bathymetric steering and trapping on the shallower (800 m) Yermak Plateau north of 80°N is indicated in Figure 9. Analysis of float trajectories north of 80°15′N shows three distinct patterns of movement (Figure 9) which were related to bottom topography. The first pattern exhibited by SOFAR floats (N1, N4, and N9) located between 100 m and 250 m on the Yermak Plateau reflects bottom-trapped motion. One of these floats (N4) displayed cyclonic motion for almost 30 days over or in close proximity to a bathymetric high of about 300 m above the surrounding depths, indicating trapping of E11. The two other floats appeared to be located within an intervening 800-m-deep saddle and cycled between two local highs, indicating weak mean advection and vorticity below 100 m. The cyclonic motion therefore disagrees with the expected anticyclonic motion over topographic highs obtained through conservation of potential vorticity.

N8 defines a trajectory possessing more steady drift to the north with the branch of AW entering the Arctic along the slope of the Yermak Plateau. Small east-west oscillations (at tidal frequencies) are very common and may become large enough to shift a float into the region of trapped motion over the Yermak Plateau.

Further west, larger meandering patterns are observed (Plate 5*a*). (Plate 5 is shown here in black and white. The color version can be found in the separate color section in this issue.) The SOFAR float trajectories within this region (N2, N7, and partly N10) suggest that the larger-scale meandering was associated with current shear and is consistent with CTD

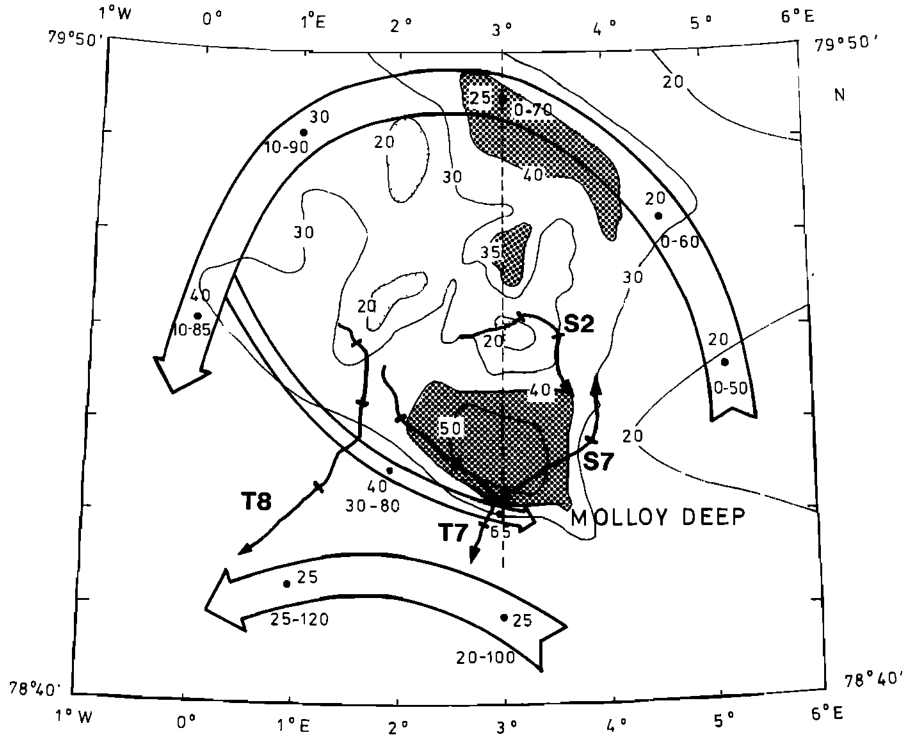

Fig. 7. Schematic of the recirculation of AW (E5) together with the bathymetry (depth in hundreds of meters), buoy trajectories and one CTD section (stippled). Numbers within the arrows indicate depth of Atlantic Water (temperature of 4°C or more). Depressions and seamounts are shown by heavy and light dotted areas, respectively.

observations and calculated dynamic height, which showed a nearly occluded meander. The meander core was AW. This meander later evolved to form a cyclonic eddy (E12) as can be seen in the closed loop patterns of the two floats and in data from independently drifting Cyclesondes (Plates 5*b* and 5*c*) that bounded the feature over a 2-week period starting July 1 [*Manley et al.*, 1986]. Ice kinematic studies from SAR mosaics [*Shuchman et al.*, 1986, also unpublished manuscript, 1986] also showed consistent cyclonic ice motion directly above this feature. The surface drift pattern of two Argos buoys deployed on ice floes confirmed the presence of the cyclonic eddy with an average orbital speed of the order of 10 cm s^{-1}.

The temperature and salinity transect of this feature (Plates 5*b* and 5*c*) with a horizontal resolution of one profile every 30 min was obtained by the southward drifting Cyclesonde as it passed near the meander core of AW (Plate 5*a*). The position of the meander was also found to coincide with a spur/trough topographic feature of similar spatial scale on the western flank of the Yermak Plateau (Figure 9) and may suggest further involvement of bottom topography in the mesoscale cyclonic eddy circulation in E12.

Off the ice edge a mesoscale eddy (E13) having a diameter of 15–20 km was mapped by R/V *Håkon Mosby* over a 10-day period from June 18 to 29, 1984 (Figures 10*a*–10*f*). For the first 3 days of this period a strong, persistent northeasterly wind of 10–15 m s^{-1} blew almost parallel to the ice edge with the ice to the right. The circular structure of the eddy is clearly evident in the depth variations of the 2.5°C isotherm and 35‰ isohaline (Figures 10*a* and 10*b*). Vertical east-west cross sections of temperature, salinity, density, and geostrophic speed with level of no motion at the surface are shown in Figures 10*c*–10*f*. The 2.5°C isotherm rises abruptly from an undisturbed mean depth of 250 m to nearly 50 m in the eddy center, leading to a separation of the AW into a core on each side. In contrast, the 34.9‰ isohaline is depressed from a depth of 75 m at the rim of the eddy to 125 m in the center.

In the surface layer a lens of cold (<2.5°C) and fresh (<34.4‰) PW with a thickness of 25 m and a width of 10 km indicates inward radial motion and convergence as a result of friction between the eddy and the overlying ice and PW. The corresponding density structure (Figure 10*e*) shows a depression of the upper layer isopycnals with reversing isopycnal slope below approximately 125 m. Thus the geostrophic flow shows cyclonic orbital motion with subsurface maximum of 20 cm s^{-1} at 125 m, located roughly 5 km off the eddy center. Except for the horizontal scale of this eddy feature, the surface lens structure located over the interior dome is in basic agreement with the eddy structure frequently observed south of 79°N. The structure and behavior of this eddy feature lead us to believe that this is an eddy in the AW advected northward with the WSC, which encountered the ice edge, leading to eddy–ice edge interaction as is shown schematically in Figure 11.

From the first observation of the feature on June 18 at the ice edge until June 26, the eddy center moved into the open ocean at 5 km d^{-1} in an easterly direction. Ice and PW trapped in the eddy during the eddy-ice interaction phase were consequently transported into warmer water by the eddy propagation. In contrast to the weak eddy movement, the ice edge retreated 50 km northward over a 4-day period owing to

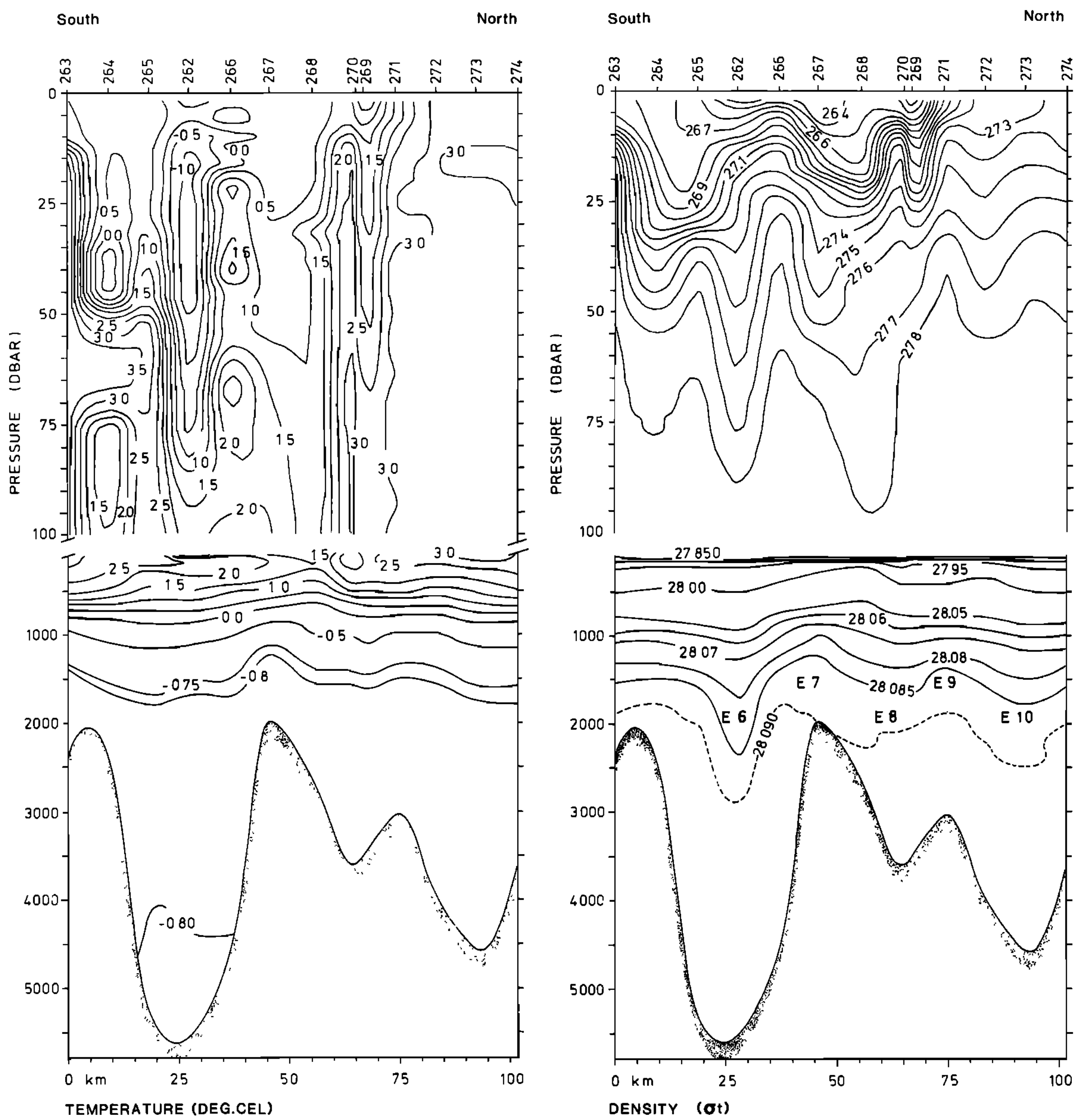

Fig. 8. (left) Temperature and (right) density structure from CTD stations (stippled CTD section in Figure 7) 263–274 indicated at the top of the section. The vertical scale of the upper 100 m is stretched.

strong southerly winds of 15 m s^{-1} beginning on June 24. From June 26 to 29 the eddy center moved eastward at 1 km d^{-1}. After this period no evidence of the eddy feature was found, indicating a decay time of 10 days.

Exploratory eddy mapping between June 27 and 29, 1984 using helicopter CTD casts below the interior ice on the east Greenland slope region showed a cyclonic eddy E14 (Figures 12*a* and 12*b*). This eddy with a geostrophic speed of 15–20 cm s^{-1} and a scale of 20–30 km was located directly south of the Ob bank, as is shown in the dynamic height contours (Figure 12*a*). In comparison, the vertical cross section of temperature, salinity, and density show an eddy about 200 m deep, and with a core more saline and denser (0.78 σ_t units) than the surrounding water (Figure 12*b*).

3. Discussion

In this section the sources and characteristics of the 14 eddies (E1–E14) identified in Fram Strait between 78°N and 81°N during MIZEX '83 and MIZEX '84 are discussed. Then the vorticity balance and energetics for a few selected eddies are analyzed. Finally, the importance of eddy-induced ablation for ice melt and retreat is quantified.

3.1. *Eddy Sources*

The general oceanographic and meteorological conditions in Fram Strait allow several eddy sources to be present on a near-permanent basis. For 7 of the 14 eddies, generation by a mixture of several sources is suggested. The generation of the others is explained by one single mechanism. Five sources leading to eddy formation can be identified:

1. The necessary condition for barotropic instability is the existence of an inflexion point in the horizontal current profile [*Pedlosky*, 1979]. During MIZEX '84 the presence of an ice edge jet in the EGC was inferred from ice floe tracking in sequential AVHRR and SAR images and from Argos drifting buoys [*MIZEX Group*, 1986]. *Vinje and Finnekåsa* [1986]

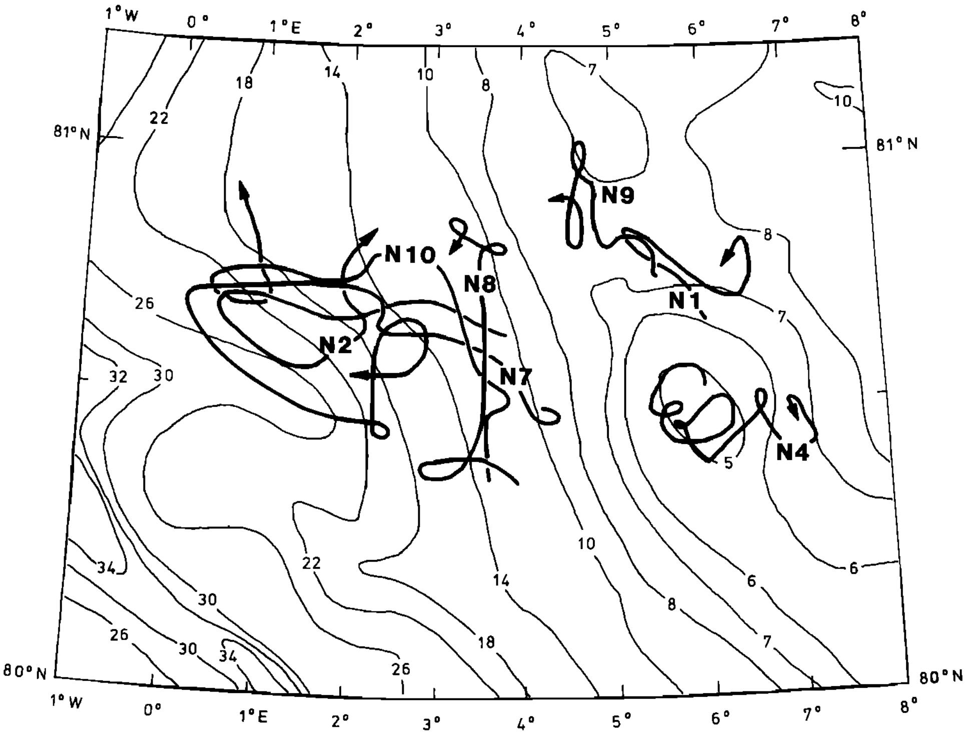

SOFAR Float	N1	N2	N4	N7	N8	N9	N10
DEPTH (m)	126	118	256	223	196	113	215

Fig. 9. SOFAR float trajectories (N1, N2, N4, N7, N8, N9, and N10) superimposed on bathymetry (depth in hundreds of meters).

have also documented the existence of this jet. Moreover, a horizontal current shear between the EGC and recirculated AW was observed south of 79°N. Less horizontal shear was found in the northern region of the strait. However, occasionally the strength of this jet and shear can increase significantly owing to wind forcing [*Johannessen et al.*, 1983]. Inflection points may be present in these shear zones, on both sides of the velocity maximum. This implies that kinetic energy can be provided to eddies through barotropic instability, favoring cyclonic eddies at the ice edge and anticyclonic eddies towards the ice interior.

2. A vertical shear between the wedge-shaped EGC and recirculated AW also exists. In addition, a baroclinic current regime in the upper ocean in the vicinity of the ice edge may be caused or enhanced by the wind driven ice edge jet as suggested in a numerical model by *Røed and O'Brien* [1983] and observed by *Johannessen et al.* [1983]. Potential energy is therefore available. In cases when the ratio of the first internal Rossby deformation radius ($R_d = h(N/f)$, i.e., the product of the vertical scale h and the ratio of Brunt-Väisälä frequency N to the Coriolis parameter f) to the width of the jet (L) is less than or equal to $O(1)$, perturbations grow through baroclinic instability [*Phillips*, 1954, *Pedlosky*, 1979]. This argument was used by *Wadhams and Squire* [1983] to conclude that the "Ymer" vortex in the EGC was generated by baroclinic instability. Thus, eddy sources 1 and 2 suggest that in the frontal regime of the EGC, baroclinic and barotropic processes combine to form mesoscale eddies.

3. Evidence of eddies generated by topographic steering and trapping due to conservation of potential vorticity is also found in Fram Strait during MIZEX '84, both in deep water in the central part of the strait and in shallow water on the Yermak Plateau.

4. Open ocean eddies present in the AW (Plate 2) are advected toward the meltwater front and the ice edge. This will lead to interaction that can develop into ice edge eddies. Furthermore, the fluid parcels must conserve potential vorticity along their path; as the AW is forced under the ice and PW, the core depth and relative distance between isopycnals increases, and so too must the relative vorticity. This may enhance formation of cyclonic eddies along the meltwater front and the ice edge.

5. Lastly, upper ocean eddies due to wind-induced differential Ekman pumping along a meandering ice edge [*Häkkinen*, 1986] have not been directly observed. However, use of Fram Strait summer conditions with a mixed layer depth of 25 m and an ice edge with meanders of 20–40 km in this model leads to formation of shallow upper layer eddies.

Table 2 summarized the characteristics for the 14 eddies E1 to E14. They are labeled as open ocean eddies (O), ice edge eddies (I), under ice eddies (U) or subsurface eddies (S). Table 2 includes information on water depth, rotation, horizontal and vertical scale, maximum orbital speed versus depth, propagation, typical vertical structure, and inferred eddy sources.

Eddies were detected in both deep and shallow water ranging from 5500 m to 250 m. Twelve of the 14 eddies were cyclonic. The mean eddy radius was 15 km $\pm$ 5 km, the only exception being E5 with a radius of 50 km. In comparison, the internal Rossby deformation radius R_d ranged between 3 and 5 km in the MIZ. The maximum observed orbital speed versus

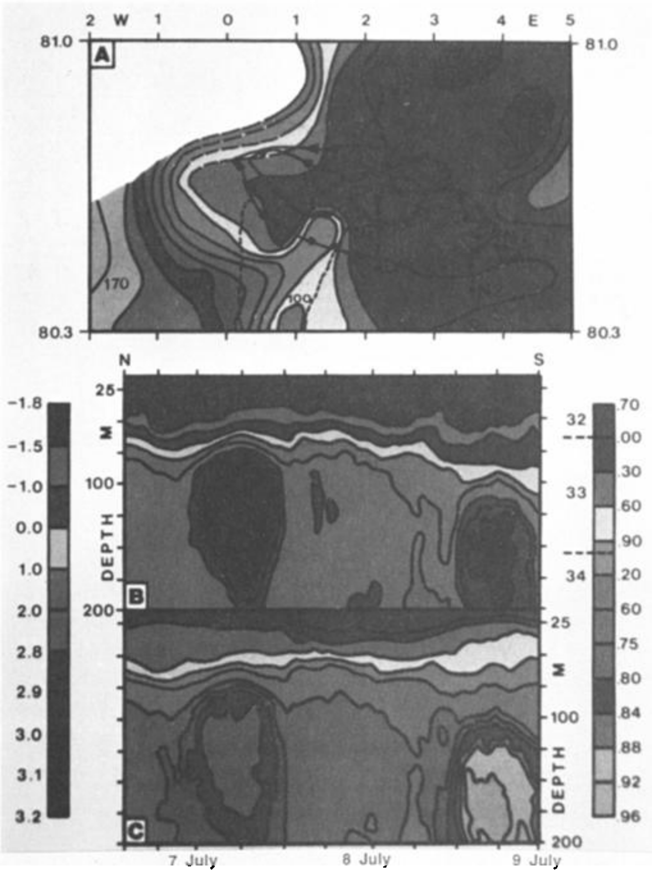

Plate 5. (*a*) SOFAR float trajectories of N2 and N7, together with surface dynamic height (contour interval of 10 dyn cm) and drift track of the Cyclesonde, with corresponding (*b*) temperature and (*c*) salinity structure from the Cyclesonde section. (The color version of this figure can be found in the separate color section in this issue.)

depth was 40 cm s^{-1} at 50 m in E1, while the deepest maximum of 20 cm s^{-1} was found at 125 m for eddy E13. These eddies are thus not categorized as submesoscale coherent vortices (SCV), which by definition have horizontal scales of less than the internal Rossby radius R_d as well as subsurface orbital velocity maxima [*McWilliams*, 1985]. The propagation speed ranged from 1 to 15 km d^{-1} for E1, and from 1 to 5 km d^{-1} for E2 to E4 and E13, while the seven eddies E5 to E11 remained trapped owing to bathymetric steering.

Table 2 suggests that the trapped eddies are generated by vorticity stretching due to flow interaction with topography (source 3) such that the cyclonic eddies (E5, E6, E8, and E10) are found over topographic depressions and the anticyclonic eddies (E7 and E9) are found over topographic highs. E5 is further enhanced by source 4. The combined effect of these six eddies can be viewed as a system with five small "gear wheels," E6 to E10, enclosed by a large gear wheel E5. The source of the trapped eddy (E11) located over the seamount on the Yermak Plateau (Figure 9) is less obvious, especially for the first 15 days. The SOFAR float deployed at 265 m displayed cyclonic orbital motion with speed ranging from 5 to 10 cm s^{-1} despite the anticyclonic motion expected from conservation of potential vorticity over a local high when the mean background vorticity is zero. It is also in disagreement with *Hunkins*' [1986] suggestion that tidal rectified vorticity waves should propagate anticyclonically around the Yermak Plateau. On the other hand, the mean cross-isobath advection toward increasing depth obtained the last 15 days displayed cyclonic orbital motion in agreement with the conservation of potential vorticity argument.

The relative importance of the six major bathymetric features in the central Fram Strait (see Figure 7) when applied in the expression for potential vorticity in a barotropic ocean on an f plane ($\zeta = [(H - H_0)/H_0]*f$) is given in Table 3. H_0 is the mean depth of the large depression of about 3000 m, and H is the depth or height of the individual features. As may be expected, the table documents that the major increase in positive relative vorticity results from the Molloy Deep, exceeding the largest increase in negative relative vorticity resulting from the seamount sited immediately north of Molloy Deep by more than 50%.

In numerical models the initial flow interaction with a topographic feature leads to the generation of a pair of eddies [*Huppert and Bryan*, 1976; *Verron and Le Provost*, 1985]. Later, a Taylor column may propagate downstream from the generation site dependent on the inverse Froude number Nh_m/U (the Brunt-Väisälä frequency N, the height of the topographic feature h_m, and the background advection U). For typical mean values in the Molloy Deep region, this number is of the order of 10 [*Smith et al.*, 1984], and the eddies will remain trapped. However, occasionally the number may decrease toward 2 for relatively strong pulsation of the mean current, U, of 50 cm s^{-1} as was observed by *Vinje and Finnekåsa* [1986]. This will lead to downstream advection of eddies. Consequently, this source (source 3) must be accounted for in the mixture of generation mechanisms for the eddies E1 to E4 located downstream of the complicated topographic region in the central part of the strait. The distance from Molloy Deep to E1 (from July 4 to 16) of about 50 km furthermore agrees with the predicted downstream wavelength to the crest of the first and largest standing wave (lee wave) from a deflection region obtained in the tank model by *Narimousa and Maxworthy* [1986]. Their results further showed that sometimes this standing wave became unstable and allowed a cyclone to pinch off from the crest. The finding of E2 about 50 km downstream of E1 is also in agreement with these tank results.

The observed circulation in the frontal region immediately south of 79°N is quasi-permanently cyclonically curved. This favors generation of cyclonic eddies [*McWilliams*, 1985] in agreement with E1 to E4. These eddies are suggested to be generated primarily by the mixture of sources 1 and 2, as is usually the case for frontal instabilities, and since a branch of the AW recirculates at 79°N, source 4 may also occur. The subsidence of the AW underneath the ice and PW in the EGC releases positive relative vorticity through density stretching. *T-S* relationships display this density stretching. Density stretching in meanders is also observed with RAFOS floats in the Gulf Stream [*Rossby et al.*, 1985]. However, trapped eddies (source 3) may occasionally be advected downstream from the Molloy Deep region in response to strong pulsation of the mean current, while standing lee waves formed downstream of Molloy Deep may also become unstable and pinch off eddies. *Paquette et al.* [1985] report on observations of a cyclonic eddy in this region with structure and scales in comparison with E1 during a field experiment in 1981. They also

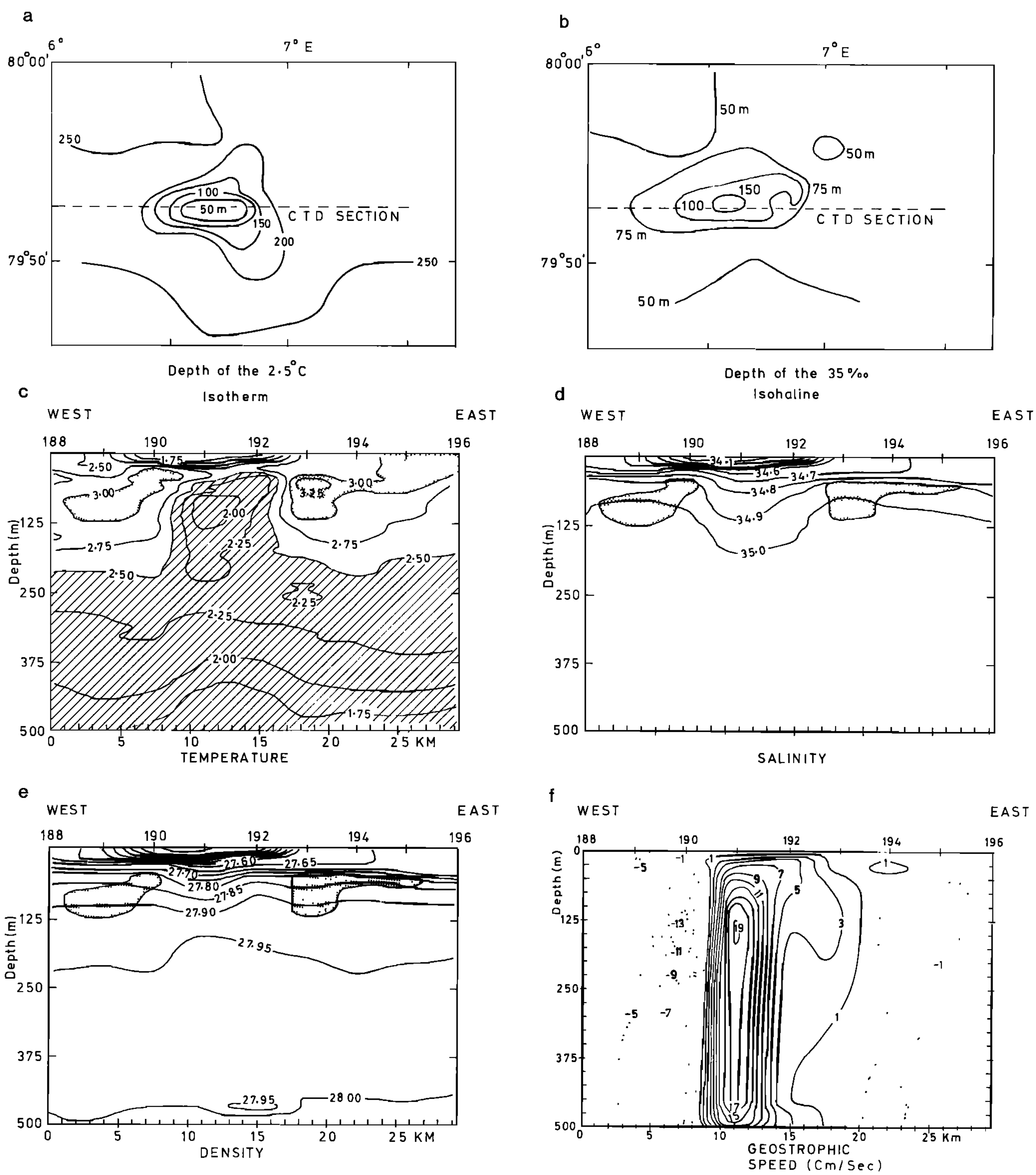

Fig. 10. Open ocean eddy E13. Horizontal plots of (*a*) 2.5°C temperature surface and (*b*) 35‰ salinity surfce; vertical structure of (*c*) temperature, (*d*) salinity, (*e*) density, and (*f*) geostrophic speed (centimeters per second) from CTD stations 188–196 indicated at the top of the sections. Northward speed is shown by solid lines.

find that other historical data in the region show a similar eddy feature.

The importance of the last eddy source (source 5) arising from differential Ekman pumping along a meandering ice edge [*Häkkinen*, 1986] needs also to be clarified. The ice advected into the central part of Fram Strait associated with E5 leads to a near-permanent meanderlike ice configuration (see Plate 2). Eddies are frequently found in the vicinity of the crest of this meander (E1 to E4 and E12). The weather maps and wind curve shown in Figure 2 also show that along ice edge winds

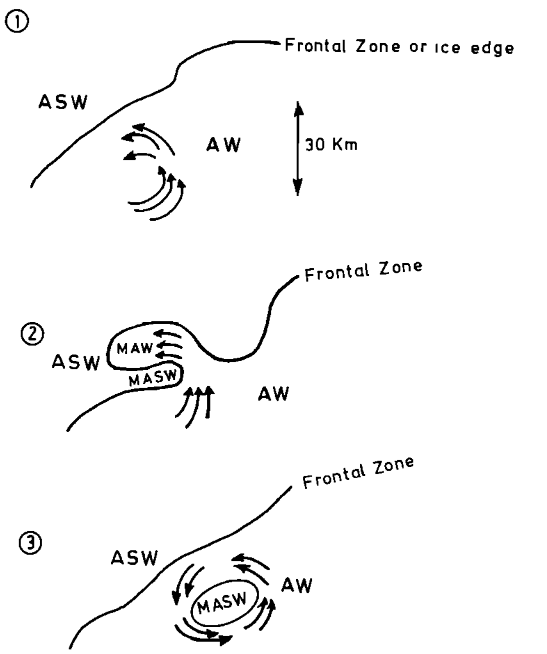

Fig. 11. Schematic of the interaction of the open ocean eddy (E13) with the ice edge.

with the ice to the right when looking downwind were common, providing favorable conditions for source 5 to generate upper ocean eddies. On the other hand, the large vertical scale of these eddies of $O(10^2\text{–}10^3$ m) cannot be explained in this way.

Finally, the detailed sampling in some of these eddies suggested that the vertical eddy structure can be divided in two categories: (1) eddies with a surface lens and interior dome structure leading to a reversal in the slope of the isopycnals, in general representative of the ice edge eddies, and (2) eddies with either upward displacement (dome structure) or downward displacement (depression) of isopycnals only. Analytical studies of joint upper ocean eddies consisting of a lens on top of a cyclonic vortex overlying an infinite deep have recently been made by *Nof* [1985]. He finds that the self-propagation of these joint upper ocean eddies is eastward when the cyclonic vortex is weak and westward when the cyclonic vortex is strong. This is in basic agreement with the observation of E13 in category 1, which propagated eastward at a maximum of 5 km/d^{-1}. The comparison with other eddies in category 1 is less satisfactory, since they are located in regions with relatively strong background circulation that dominates the eddy propagation.

3.2. *Vorticity Balance*

Scaling of the potential vorticity equation for a stratified ocean enables the relative importance of the various terms in the dynamic relationship of the eddies to be quantified and analysed. E1, E12, E13, and E14 were selected for this study. The CTD data and current meter data are used in the calculations. The ageostrophic effect (friction) that leads to surface convergence in several of the ice edge eddies is neglected in this scaling argument.

In accordance with *Olson* [1980] the potential vorticity equation in cylindrical coordinates on an f plane can be approximated by

$$D/dt\ \{-(\partial\rho/\partial r)(\partial v/\partial z) + \partial\rho/\partial z\ (v/r + \partial v/\partial r + f)\} = 0 \qquad (1)$$

where v and ρ are the mean horizontal speed and density, and the vertical velocity is negligible in comparison with v, and derivatives in azimuthal directions are much smaller than those in radial directions. The inner parenthesis of the second term contains the relative and planetary vorticity terms multiplied by the density stratification, while the first term accounts for the radial vorticity. In Table 4 these source terms are quantified in order of magnitude.

Apparently, for all four eddies most of the adjustment is in the second term. Thus in order for a fluid parcel to conserve potential vorticity, an increase in relative vorticity associated with the cyclonic turn must be accompanied by a stretching of isopycnals. Water parcels will thereby downwell along density surfaces as they are advected cyclonically through the feature.

3.3. *Energetics*

The supply of kinetic energy through barotropic instability arises from Reynolds stresses working against the mean horizontal velocity gradient [*Pedlosky*, 1979], i.e., $E_k = -u'v'\partial v/\partial x$, where u', v' are the perturbation velocities. A corresponding expression for the available potential energy released through baroclinic instability is $E_p = -(g/\rho_0 N)^2(u'\rho'\partial\rho/\partial x)$, showing that the potential energy arises through the advection of density perturbation across the mean horizontal density gradient. Following *Thomson* [1984] the relative importance of these two source terms is scaled as

$$S = E_p/E_k = (fg/N^2)(\rho'/\rho_0)(L/H)v'^{-1} = 2(\rho'/v') = 1 \qquad (2)$$

for realistic input values (in mks units) of $f = 1.4 \times 10^{-4}$ s^{-1}, $g = 10$ m s^{-2}, $N^2 = 3 \times 10^{-5}$ s^{-2}, $\rho_0 = 10^3$ kg m^{-3}, $L = 20$ km, and $H = 500$ m, and values of ρ' and v' of 0.1 kg m^{-3} and 0.2 m s^{-1} at the depth of maximum orbital speed (see Figures 4 and 6). Alternatively, using the thermal wind relationship of the perturbation ($fv'/H \approx \rho' g/\rho_0 L$) this ratio can be written $S = (f/N)^2\ (L/H)^2$, which also equals 1. Equal contributions of 50% from the potential and the kinetic energy exchange from the mean to the "perturbation" eddy field are thus expected. In comparison, similar scaling applied to a Gulf Stream ring [*Thomson*, 1984] indicates that 90% of the energy exchange is associated with the baroclinic term.

The mean available potential energy (APE) and kinetic energy (KE) in E1 was also roughly calculated using the CTD data shown in Figure 4 with the assumption that the eddy was symmetric. From *Olson* [1980] the APE is estimated using the integral

$$\text{APE} = g/2 \int_r^0 \int_{500}^0 (\partial\rho/\partial z)(h_i - h_r)^2\, dz\, dr \qquad (3)$$

where h_i is the depth of the density surface in the eddy and h_r is the reference depth of the same surface. The kinetic energies are estimated using

$$\text{KE} = \rho/2 \int_r^0 \int_{500}^0 v^2\, dz\, dr \qquad (4)$$

where the velocities are calculated from the gradient current balance with input of calculated geostrophic speed, and with no account of the barotropic eddy speed. The integration is from the surface to the general CTD sampling depth of 500 m.

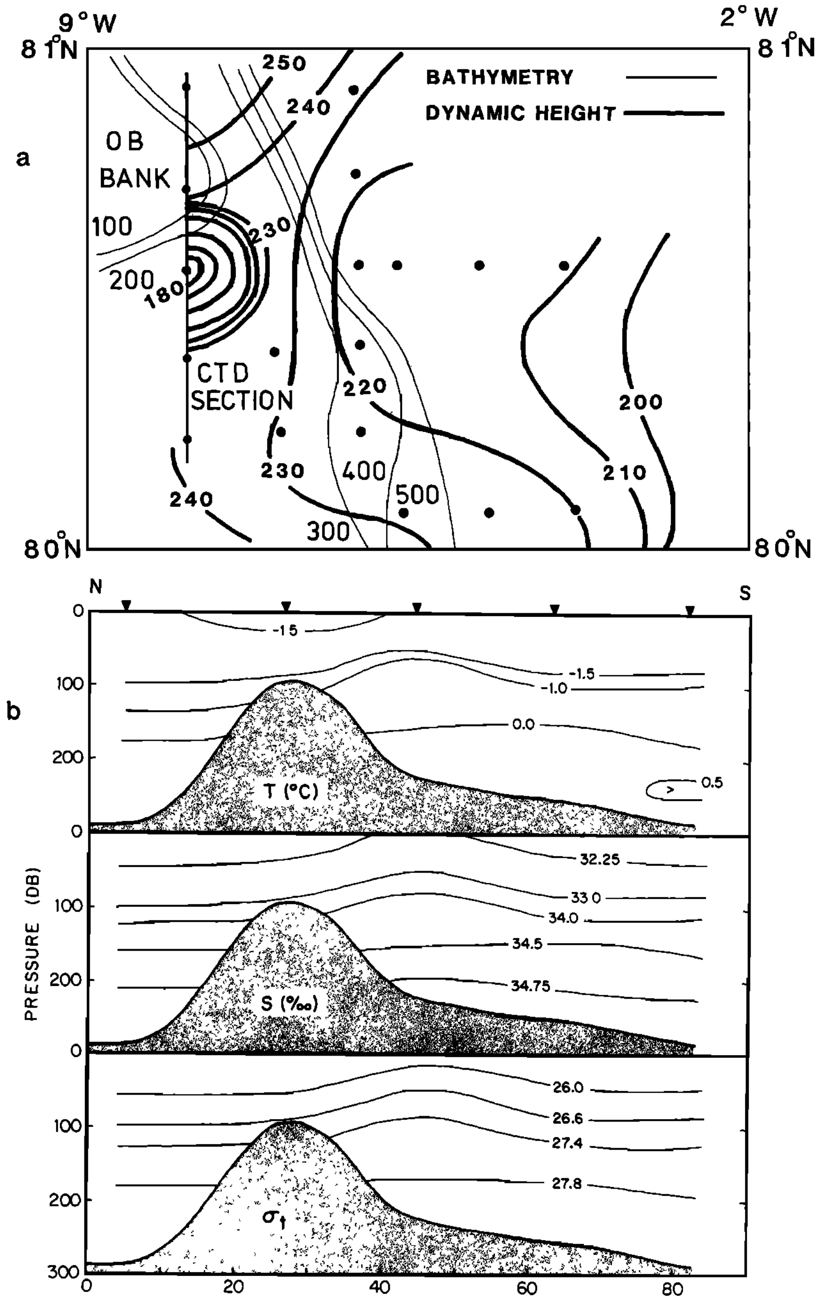

Fig. 12. (*a*) Horizontal plot of the surfce dynamic height (contour interval 10 dyn cm), north-south CTD section crossing the Ob bank, bathymetry (contour interval of 100 m) and CTD station positions (solid dots). (*b*) Temperature, salinity, and density structure from CTD section (stations marked at top of section).

In contrast to the result of formula (2), the ratio of available potential energy to kinetic energy in E1 is 5, with peak APE and KE both located approximately 10 km off the center. Complete agreement is not necessarily expected between the ratio of potential and kinetic energy transfer and the ratio of potential and kinetic energy distribution. On the other hand, if a rough estimate of the KE contribution from deeper water (barotropic speed ≈ 0.10 m s^{-1} for eddy E1) is accounted for, the ratio (APE/KE) decreases to approximately 2, in closer agreement with the results obtained from the scaling argument using formula (2).

3.4. *Eddy-Induced Ablation*

The abundant eddies along the ice edge not only advect warm AW beneath the ice but also sweep ice and PW out away from the pack into warmer AW. Both of these processes greatly accelerate ice ablation by bringing warm water into contact with the ice. In these conditions, the bottom ablation, as measured during MIZEX '83 and MIZEX '84 [*Josberger*, this issue] attains values from 0.25 to 0.5 m d^{-1} compared to 0.01–0.02 m d^{-1} for the interior ice pack.

To estimate the effect of eddy heat transport on the ice edge, consider the following simple case. A series of eddies is cen-

TABLE 2. Characteristics of the 14 Eddies, E1–E14

Eddy	Water Depth, m	Rotation	Radius, km	Vertical Scale, m	Maximum Speed/Depth, cm s^{-1}/m	Propagation, km d^{-1}	Structure	Source
				South of 79°N				
E1 (I)	2400	cyclonic	15	1000	40/50	1–15	surface lens/ interior dome	1, 2 (3)
E2 (I)	2400	cyclonic	15			1–5		1, 2 (3)
E3 (O)	2600	cyclonic	15	>500	40/0	1–5	dome	1, 2 (3)
E4 (O)	2400	cyclonic	20	>500	30/0	1–5		1, 2 (3)
				79°–80°N				
E5	3000	cyclonic	50	1000		trapped		3, 4
E6 (I, S)	5500	cyclonic	20	5400		trapped	depression	3
E7 (I, S)	1400	anticyclonic	15	1300		trapped	dome	3
E8 (I, S)	4000	cyclonic	15	3900		trapped	depression	3
E9 (I, S)	3000	anticyclonic	15	2800		trapped	dome	3
E10 (S)	4500	cyclonic	15	4300		trapped	depression	3
				North of 80°N				
E11 (U)	500	cyclonic	10	300		trapped		3
E12 (U)	2000	cyclonic	15	>200	10/0	negligible		4
E13 (O)	1200	cyclonic	10	400	20/125	1–5	surface lens/ interior dome	4
E14 (U)	250	cyclonic	15	200	20/0		dome	1, 2

The maximum orbital speed is either geostrophically calculated or directly measured. Eddy types are as follows: O, open ocean eddy; I, ice edge eddy; U, under ice eddy; S, subsurface eddy.

tered along the ice edge, the eddy centers are separated by a distance l, and each eddy has a radius r. Then the eddy will bring $\pi^* r^2/2$ m^2 of ice in contact with warm water of 3°–4°C. If the ice is h m thick and melts at w m d^{-1}, then the average retreat of the ice edge of the distance l is given by

$$A = (w\pi r^2)/(2lh) \tag{5}$$

For typical MIZ values, $r = 15$ km, $h = 1.5$ km, $l = 50$ km, the ice edge melt will be about 1 to 2 km d^{-1}.

Additional effects include weakening of the ice which makes it more susceptible to destruction by floe collisions and surface wave breakup. The fact that only ice floes approximately 200 m across and never large floes (>1 km) are observed in the eddies substantiates the importance of this process. The reduced ice concentration in the eddies increases the absorption of solar radiation, replacing the heat lost by melting. The relatively small ice floes in eddies also have greater ratios of lateral area to bottom area than do larger floes; hence lateral ablation becomes important.

4. CONCLUSIONS

Observations and interpretations of the summer MIZEX '83–MIZEX '84 eddy investigation in Fram Strait between Svalbard and Greenland lead to the following conclusions:

TABLE 3. Conservation of Potential Vorticity Relative to the Six Major Topographic Features in Central Fram Strait Shown in Figure 7

Feature	H, m	$H - H_0$, m	ζ
Depression 1	4500	1500	$0.5f$
Depression 2	3600	600	$0.2f$
Depression 3 (Molloy Deep)	5500	2500	$0.83f$
Seamount 1	1500	−1500	$-0.5f$
Seamount 2	1500	−1500	$-0.5f$
Seamount 3	1400	−1600	$-0.53f$

Mesoscale eddies are found both in shallow water with depths of several hundred meters and in deep water with depths of several thousand meters and have typical scales of 30–40 km. The majority of the eddies rotate cyclonically with maximum orbital speed, in some cases subsurface, of approximately 40 cm s^{-1}. Observations further suggest that the eddy propagation is dominated by the advection within the background mean flow reaching up to 15 km d^{-1}, and that the eddy lifetime is at least 20–30 days.

Five independent ice-ocean eddy sources are present. The topographically controlled eddies are basically formed by conservation of potential vorticity as the barotropic flow component interacts with the bathymetry. Occasionally, these trapped eddies may be advected downstream in response to strong pulsation of the mean current. However, the transient eddies along the frontal zone and ice edge are primarily formed by a mixture of barotropic and baroclinic instability. Additionally, the abundance of eddies along the ice edge may increase owing to interaction of AW eddies with the ice edge and vorticity stretching as the AW is forced under the PW, as well as owing to differential Ekman pumping.

The major terms in the vorticity balance estimated for several of the best sampled eddies are associated with the stretching of isopycnals and the accompanying changes in the radial shear in combination with the Coriolis parameter. In comparison the contribution from the first term in equation (1) is at least an order of magnitude less, which indicates the relative importance of these terms in modeling. However, the ice convergence in the center of the eddies indicates that the frictional forces, not included in the vorticity equation, must also be considered in modeling.

The energy distribution in the eddy feature E1 indicates that the available potential energy exceeds the kinetic energy by a factor of about 2. However, the data did not allow the temporal decrease in the APE, and thus eddy decay or spindown, to be quantified. Furthermore, the abundance of the eddies also suggests that energy transfer by eddy-eddy interaction is important and must be included in modeling.

The abundance of eddies enhances the ablation during

TABLE 4. Quantification of Source Terms in Equation of Potential Vorticity on a f Plane

Eddy	Radius, km	Maximum Speed, m s^{-1}	Vertical Scale, m	$\partial\rho/\partial r$, kg m^{-4}	$\partial\rho/\partial z$, kg m^{-4}	$\partial v/\partial r + v/r$, s^{-1}	$\partial v/\partial z$, s^{-1}	f, s^{-1}	Term 1, kg m^{-4} s^{-1}	Term 2, kg m^{-4} s^{-1}
E1	15	0.40	1000	0.5×10^{-4}	2.0×10^{-2}	0.3×10^{-4}	0.4×10^{-2}	1.4×10^{-4}	2.0×10^{-7}	30.0×10^{-7}
E12	15	0.10	>200	0.5×10^{-4}	1.0×10^{-2}	0.1×10^{-4}	0.05×10^{-2}	1.4×10^{-4}	0.25×10^{-7}	10.0×10^{-7}
E13	7	0.20	400	0.4×10^{-4}	4.0×10^{-2}	0.3×10^{-4}	0.2×10^{-2}	1.4×10^{-4}	0.8×10^{-7}	70.0×10^{-7}
E14	15	0.20	200	0.3×10^{-4}	1.5×10^{-2}	0.2×10^{-4}	0.2×10^{-2}	1.4×10^{-4}	0.6×10^{-7}	20.0×10^{-7}

Term 1, $(\partial\rho/\partial r)(\partial v/\partial z)$. Term 2, $(\partial\rho/\partial z)(v/r + \partial v/\partial r + f)$.

summer by 1–2 km of ice edge melt per day, and is a thermodynamic process which needs to be included in ice edge modeling.

Acknowledgments. The authors wish to express their gratitude to I. Dyer, B. Farrelly, P. Gloersen, K. Kloster, D. Ross, P. Piau and T. Tørresen, who participated and contributed via workshops. Thanks also to the crew onboard the remote sensing aircraft CV 580 and B-17 and research vessles *Håkon Mosby*, *Kvitbjørn*, *Polarstern* and *Polarbjørn*. The MIZEX program reported in this paper was funded by the University of Bergen, Norway; Royal Norwegian Council for Scientific and Industrial Research, Space Activity Division (NTNF-R); Norwegian Research Council for Science and Humanities (NAVF); and Office of Naval Research contracts provided by the Arctic Programs to the Geophysical Institute, Division A/Nansen Remote Sensing Center, University of Bergen, Norway; Environmental Research Institute of Michigan; Columbia University; Naval Postgraduate School; University of Miami; and U.S. Geological Survey and by European Community Commission contract CCE CLI-083 F, Centre National Recherche Scientifique/Pirocean 981022 and Centre National Exploitation des Oceans contract 84-3147 to the Laboratoire d'Oceanographie Physique, Paris.

REFERENCES

Aagaard, K., and P. Greissman, Toward a new mass and heat budget for the Arctic Ocean, *J. Geophys. Res.*, *80*, 3821–3827, 1975.

Häkkinen, S., Ice banding as a response of the coupled ice-ocean system to temporally varying winds, *J. Geophys. Res.*, *91*, 5047–5053, 1986.

Hunkins, K., Anomalous tidal currents on the Yermak Plateau, *J. Mar. Res.*, *44*, 51–69, 1986.

Huppert, H. E., and K. Bryan, Topographically generated eddies, *Deep Sea Res.*, *23*, 655–679, 1976.

Johannessen, O. M., J. A. Johannessen, J. Morison, B. A. Farrelly, and E. A. S. Svendsen, Oceanographic conditions in the marginal ice zone north of Svalbard in early fall 1979 with an emphasis on mesoscale processes, *J. Geophys. Res.*, *88*, 2755–2769, 1983.

Johannessen, O. M., J. A. Johannessen, B. Farrelly, K. Kloster, and R. A. Shuchman, Eddy studies during MIZEX 83 by ship and remote sensing observations, Proceedings of the 1984 International Geoscience and Remote Sensing Symposium, *Eur. Space Agency Spec. Publ.*, *ESASP-215*, 365–368, 1984.

Josberger, E. G., Bottom ablation and heat transfer coefficients from the 1983 Marginal Ice Zone Experiments, *J. Geophys. Res.*, this issue.

Killworth, P D., and N. Paldor, A model of sea-ice front instabilities, *J. Geophys Res.*, *90*, 883–888, 1985.

Magaard, L., P. Muller, and R. Pujalet, The role of eddies in the general ocean circulation, Proceedings, Hawaiian Winter Workshop, Hawaii Inst. Geophys. Spec. Publ., 359 pp., Univ. of Hawaii, Manoa, 1983.

Manley, T. O., J. Z. Villanueva, J. C. Gascard, P. F. Jeannin, K. L. Hunkins, and J. Van Leer, Mesoscale oceanographic processes beneath the ice of Fram Strait, *Science*, in press, 1986.

McWilliams, J. C., Submesoscale coherent vortices in the ocean, *Rev. Geophys.*, *23*, 165–182, 1985.

MIZEX Group, MIZEX East 83/84: The summer marginal ice zone program in the Fram Strait/Greenland Sea, *Eos Trans. AGU*, *67*, 513–517, 1986.

Narimousa, S., and T. Maxworthy, Laboratory modeling of coastal upwelling, *Eos Trans. AGU*, *67*, 2–4, 1986.

Nof, D., Joint vortices, eastward propagating eddies and migratory Taylor columns, *J. Phys. Oceangr.*, *15*, 1114–1137, 1985.

Olson, D. B., The physical oceanography of two rings observed by the Cyclonic Ring Experiment, II, Dynamics, *J. Phys. Oceanogr.*, *10*, 514–528, 1980.

Paquette, R. G., R. Bourke, J. F. Newton, and W. Perdue, The east Greenland polar front in autumn, *J. Geophys. Res.*, *90*, 4866–4882, 1985.

Pedlosky, J., *Geophysical Fluid Dynamics*, 624 pp., Springer, New York, 1979.

Perkin, R. G., and E. L. Lewis, Mixing in the West Spitzbergen Current, *J. Phys. Oceanogr.*, *14*, 1315–1325, 1984.

Phillips, N. A., Energy transformations and meridional circulations associated with simple baroclinic waves in a two-level, quasi-geostrophic model, *Tellus*, *6*, 273–280, 1954.

Quadfasel, D., J.-C. Gascard, and K.-P. Koltermann, Large-scale oceanography in Fram Strait during the 1984 Marginal Ice Zone Experiment, *J. Geophys. Res.*, this issue.

Robinson, A. (Ed.), *Eddies in Marine Science*, 609 pp., Springer, New York, 1983.

Rossby, T., A. S. Bower, and P. T. Shaw, Particle pathways in the Gulf Stream, *Bull. Am. Meteorol. Soc.*, *66*, 1106–1110, 1985.

Røed, L. P., and J. J. O'Brien, A coupled ice-ocean model of upwelling in the marginal ice zone, *J. Geophys. Res.*, *88*, 2863–2872, 1983.

Shuchman, R. A., B. A. Burns, O. M. Johannessen, E. G. Josberger, W. J. Campbell, T. Manley, and N. Lannelongue, Remote sensing of the Fram Strait marginal ice zone, *Science*, in press, 1986.

Smith, D. C., IV, J. H. Morison, J. A. Johannessen, and N. Untersteiner, Topographic generation of an eddy at the edge of the East Greenland Current, *J. Geophys. Res.*, *89*, 8205–8208, 1984.

Swift, J. H., *The Nordic Seas*, edited by B. G. Hurtle, pp. 129–153, Springer, New York, 1986.

Swift, J. H., and K. Aagaard, Seasonal transitions and water mass formation in the Iceland and Greenland seas, *Deep Sea Res.*, *28*, 1107–1129, 1981.

Thomson, R. E., A cyclonic eddy over the continental margin of Vancouver Island: Evidence for baroclinic instability, *J. Phys. Oceanogr.*, *14*, 1326–1450, 1984.

Verron, J., and C. Le Provost, A numerical study of quasi-geostrophic flow over isolated topography, *J. Fluid Mech.*, *154*, 231–252, 1985.

Vinje, T., Sea ice studies in the Spitzbergen-Greenland area, *Landsat Rep. E77-10206*, 45 pp., U.S. Dep. of Commer., Washington, D. C., 1977. (Available as NTIS 28540, Natl. Tech. Inf. Serv., Springfield, Va.)

Vinje, T., and Ø. Finnekåsa, The ice transport through the Fram Strait, *Skr. Norsk Polarinst.*, *186*, 39 pp., 1986.

Wadhams, P., and V. A. Squire, An ice-water vortex at the edge of the East Greenland current, *J. Geophys. Res.*, *88*, 2770–2780, 1983.

W. J. Campbell and E. Josberger, U.S. Geologial Survey, University of Puget Sound, Tacoma, WA 98416.

K. Davidson, Naval Postgraduate School, Monterey, CA 93940.

J. C. Gascard, Laboratoire d'Océanographie Physique, Muséum d'Histoire Naturelle, 43, rue Cuvier, 75231 Paris, Cedex 05, France.

J. A. Johannessen, O. M. Johannessen, T. Olaussen, S. Sandven, and E. Svendsen, Nansen Remote Sensing Center, Edvard Griegsvei 3A, 5037 Solheimsvik, Bergen, Norway.

T. Manley, Lamont-Doherty Geological Observatory, Columbia University, Palisades, NY 10964.

R. Shuchman, Environmental Research Institute of Michigan, Ann Arbor, MI 48107.

J. Van Leer, Department of Oceanography, University of Miami, Miami, FL 33149.

(Received November 6, 1986;
accepted January 15, 1987.)

Plate 1 [*Johannessen et al.*]. Aerial photograph of the 20- to 40-km ice edge eddy E1 centered at 79°N, 2°30′W taken from the CV 580 on June 30, 1984.

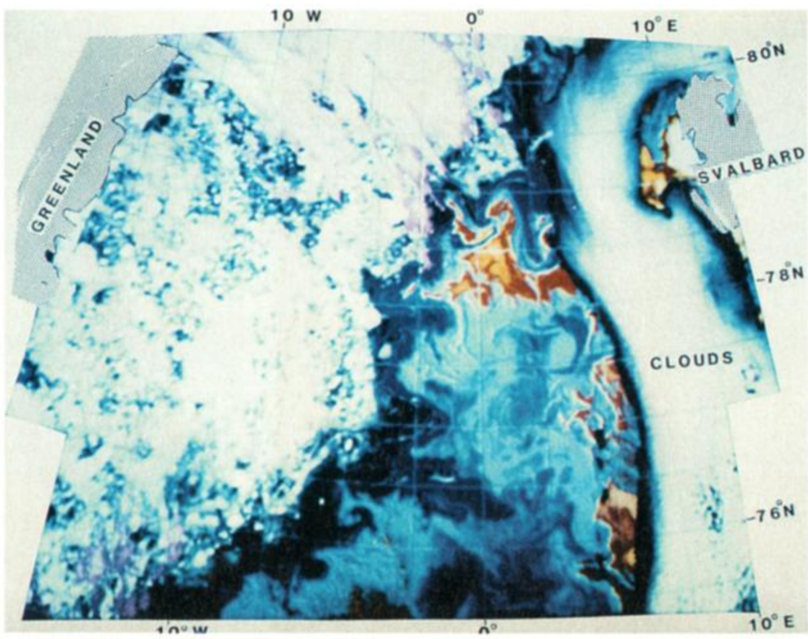

Plate 2 [*Johannessen et al.*]. NOAA satellite AVHRR image (combined IR and visual) from July 1, 1984. The temperature color scale in the ocean ranges from blue (0°C) to yellow (4°C). The albedo gray scale of the ice ranges from black (ice edge) to white (ice pack). Clouds west of Svalbard are also white. (This image was processed at Christian Michelsens Institute, Bergen, Norway, by K. Kloster.)

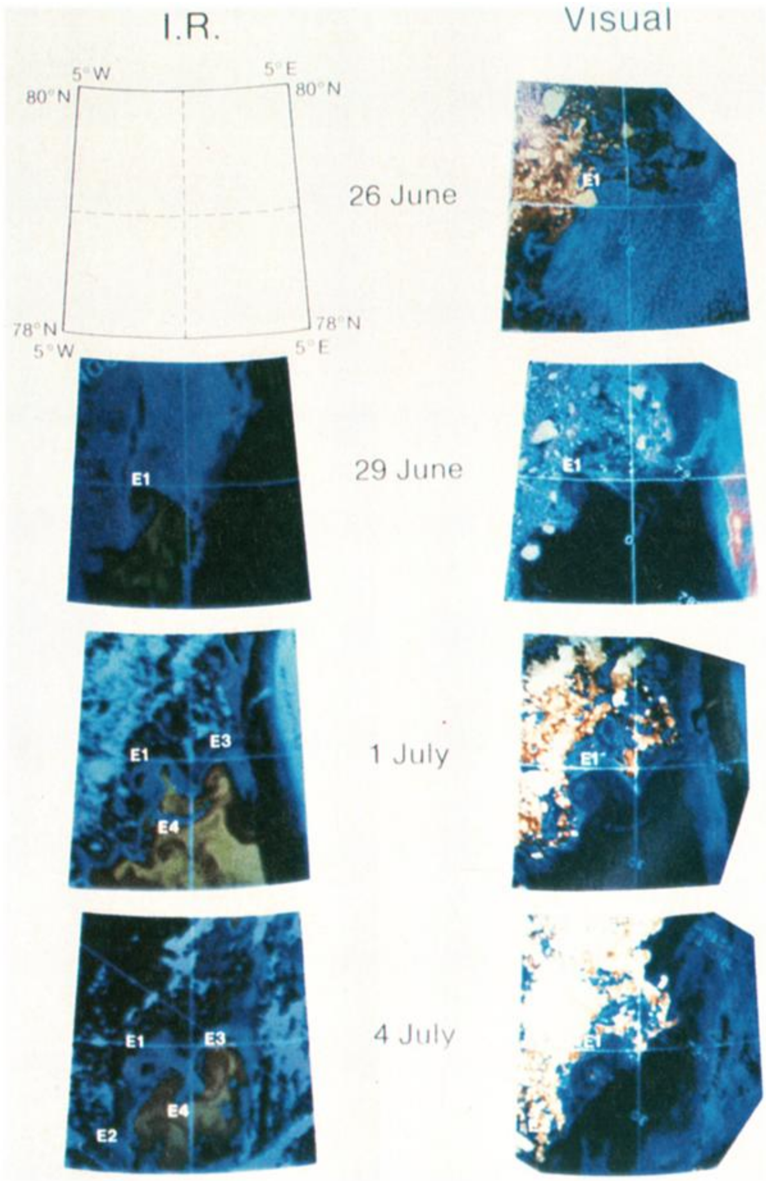

Plate 3*a*

Plate 3 [*Johannessen et al.*]. Sequence of NOAA satellite visual and IR images on June 26, June 29, July 1, and July 4; aircraft SAR mosaics on July 5, 7, and 9; and SLAR mosaic on July 14. Eddy features labeled E1–E4 are discussed in the text.

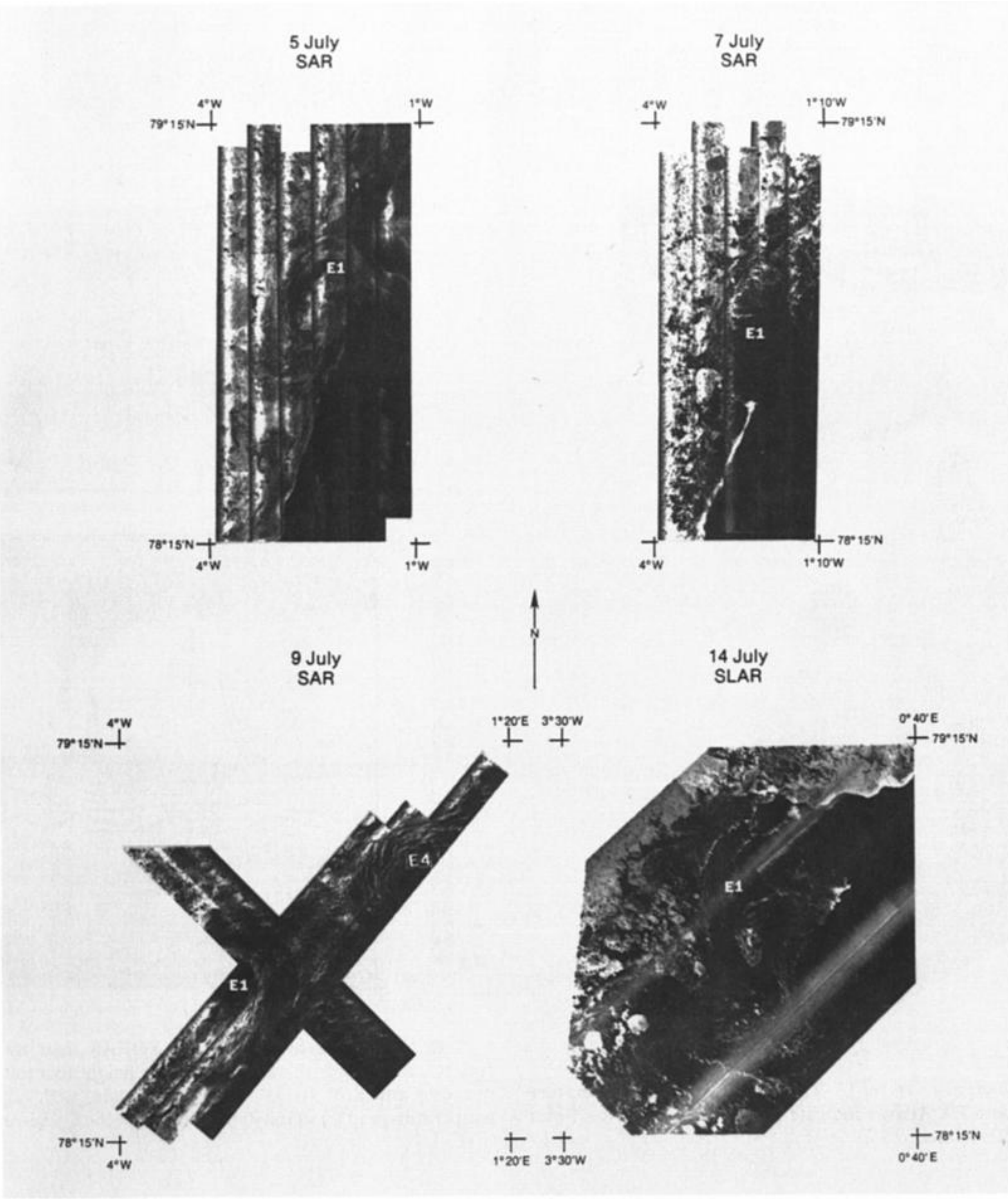
5 July
SAR
4°W
1°W
79°15'N
E1
78°15'N
4°W
1°W
7 July
SAR
4°W
1°10'W
79°15'N
E1
78°15'N
4°W
1°10'W
N
9 July
SAR
4°W
79°15'N
1°20'E
3°30'W
E4
E1
78°15'N
4°W
1°20'E
3°30'W
14 July
SLAR
0°40'E
79°15'N
E1
78°15'N
0°40'E

Plate 3*b*

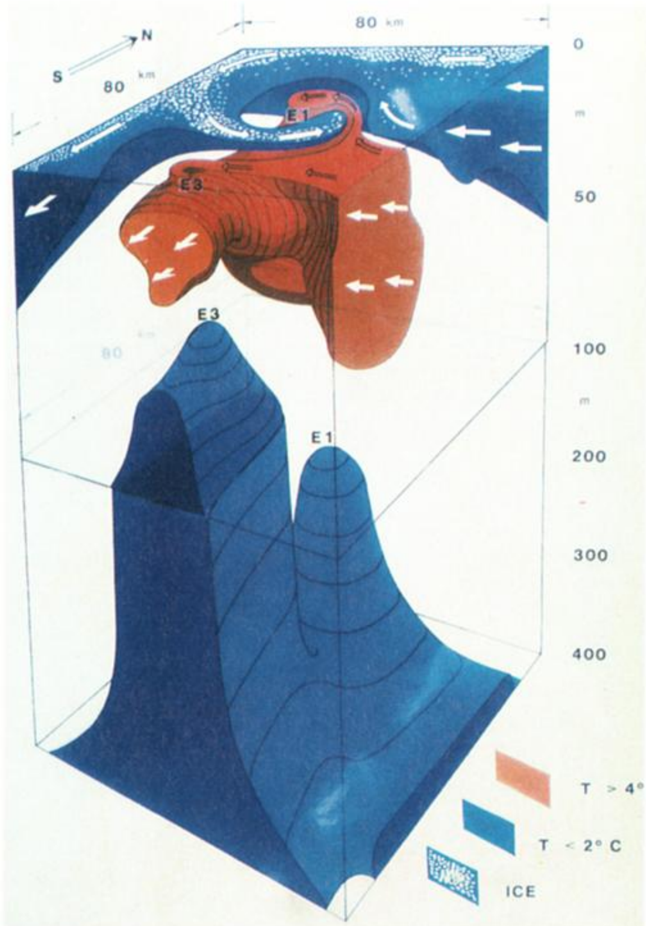

Plate 4 [*Johannessen et al.*]. Three-dimensional temperature composite of E1 and E3. Arrows indicate the motions of the ice, Polar Water, and Atlantic Water.

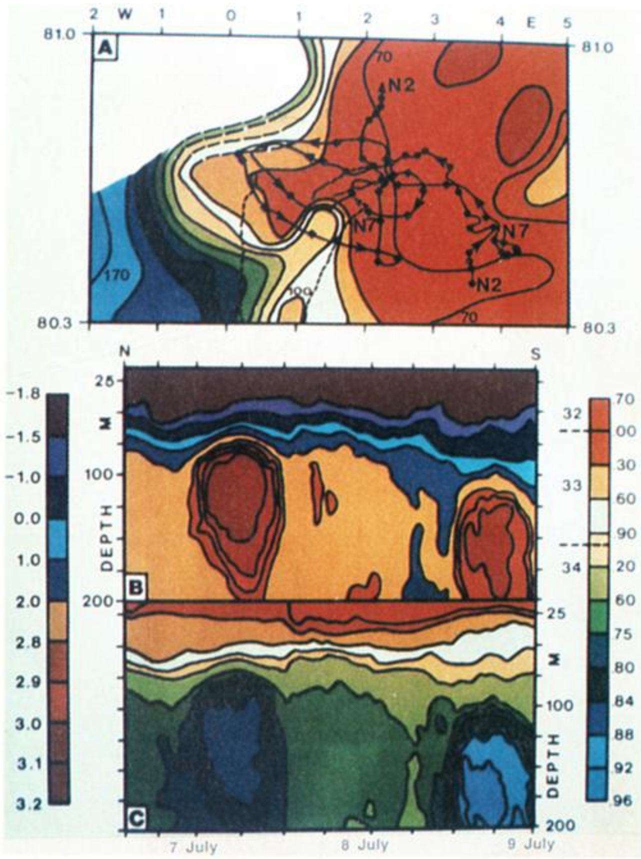

Plate 5 [*Johannessen et al.*]. (*a*) SOFAR float trajectories of N2 and N7, together with surface dynamic height (contour interval of 10 dyn cm) and drift track of the Cyclesonde, with corresponding (*b*) temperature and (*c*) salinity structure from the Cyclesonde section.